



**HAL**  
open science

## Characterization of the first tetrameric transcription factor of the GntR superfamily with allosteric regulation from the bacterial pathogen *Agrobacterium fabrum*

Armelle Vigouroux, Thibault Meyer, Anaïs Naretto, Pierre Legrand, Magali Aumont-Nicaise, Aurélie Di cicco, Sébastien Renoud, Jeanne Doré, Daniel Lévy, Ludovic Vial, et al.

### ► To cite this version:

Armelle Vigouroux, Thibault Meyer, Anaïs Naretto, Pierre Legrand, Magali Aumont-Nicaise, et al.. Characterization of the first tetrameric transcription factor of the GntR superfamily with allosteric regulation from the bacterial pathogen *Agrobacterium fabrum*. *Nucleic Acids Research*, 2021, 49 (1), pp.529-546. 10.1093/nar/gkaa1181 . hal-03367389

**HAL Id: hal-03367389**

**<https://hal.science/hal-03367389>**

Submitted on 6 Oct 2021

**HAL** is a multi-disciplinary open access archive for the deposit and dissemination of scientific research documents, whether they are published or not. The documents may come from teaching and research institutions in France or abroad, or from public or private research centers.

L'archive ouverte pluridisciplinaire **HAL**, est destinée au dépôt et à la diffusion de documents scientifiques de niveau recherche, publiés ou non, émanant des établissements d'enseignement et de recherche français ou étrangers, des laboratoires publics ou privés.

1 **Characterization of the first tetrameric transcription factor of the**  
2 **GntR superfamily with allosteric regulation from the bacterial**  
3 **pathogen *Agrobacterium fabrum***

4 Armelle Vigouroux<sup>1†</sup>, Thibault Meyer<sup>2†</sup>, Anaïs Naretto<sup>1#</sup>, Pierre Legrand<sup>3</sup>, Magali Aumont-Nicaise<sup>1</sup>,  
5 Aurélie Di Cicco<sup>4</sup>, Sébastien Renoud<sup>2</sup>, Jeanne Doré<sup>2</sup>, Daniel Lévy<sup>4</sup>, Ludovic Vial<sup>2</sup>, Céline Lavire<sup>2\*</sup>,  
6 Solange Moréra<sup>1\*</sup>

7 1 Université Paris-Saclay, CEA, CNRS, Institute for Integrative Biology of the Cell (I2BC), 91198, Gif-  
8 sur-Yvette, France

9 2 Université Claude Bernard Lyon 1, CNRS, INRAE, VetAgro Sup, UMR Ecologie Microbienne, 69622  
10 Villeurbanne, France

11 3 Synchrotron SOLEIL, L'Orme des Merisiers, Saint-Aubin, 91192, Gif-sur-Yvette, France

12 4 Laboratoire Physico Chimie Curie, Institut Curie, PSL Research University, CNRS UMR 168, Paris  
13 75005, France

14 #Present Address: Anaïs Naretto, Department of Biochemistry, Vanderbilt University, Nashville,  
15 Tennessee, 37235, USA

16 † These authors contributed equally to this work

17 \* To whom correspondence should be addressed. Tel: +33169824213; E-mail:  
18 solange.morera@i2bc.paris-saclay.fr; Tel: +33426237126 celine.lavire@univ-lyon1.fr

19  
20 **ABSTRACT**

21 A species-specific region, denoted SpG8-1b allowing hydroxycinnamic acids (HCAs) degradation is  
22 important for the transition between the two lifestyles (rhizospheric versus pathogenic) of the plant  
23 pathogen *Agrobacterium fabrum*. Indeed, HCAs can be either use as trophic resources and/or as  
24 induced-virulence molecules. The SpG8-1b region is regulated by two transcriptional regulators, namely,  
25 HcaR (Atu1422) and Atu1419. In contrast to HcaR, Atu1419 remains so far uncharacterized. The high-  
26 resolution crystal structures of two fortuitous citrate complexes, two DNA complexes and the apoform  
27 revealed that the tetrameric Atu1419 transcriptional regulator belongs to the VanR group of Pfam  
28 PF07729 subfamily of the large GntR superfamily. Until now, GntR regulators were dimeric. Here, we  
29 showed that Atu1419 represses three genes of the HCAs catabolic pathway. We characterized both  
30 the effector and DNA binding sites and identified key nucleotides in the target palindrome. From  
31 promoter activity measurement using defective gene mutants, structural analysis and gel-shift assays,  
32 we propose N<sup>5</sup>,N<sup>10</sup>-methylene tetrahydrofolate as the effector molecule, which is not a direct  
33 product/substrate of the HCA degradation pathway. The Zn<sup>2+</sup> ion present in the effector domain has  
34 both a structural and regulatory role. Overall, our work shed light on the allosteric mechanism of  
35 transcription employed by this GntR repressor.

37

38

## 39 INTRODUCTION

40 *Agrobacterium fabrum* has two lifestyles: it can interact with a large variety of plants as a rhizosphere  
41 inhabitant or as a pathogen when it harbors a tumor-inducing plasmid (which is a virulence plasmid),  
42 and transfers a portion of this to the plant cells upon infection, resulting in the crown-gall disease (1-3).  
43 *A. fabrum* possesses a species-specific region, denoted SpG8-1b (a region present in strains of this  
44 species but absent from other *Agrobacterium* species), located in the circular chromosome and  
45 responsible for hydroxycinnamic acids (HCAs) degradation such as ferulic acid, caffeic acid and *p*-  
46 coumaric acid (4,5) (Figure 1). These latter compounds are common plant secondary metabolites being  
47 precursors of lignin incorporated into plant cell walls. They are abundantly released in soil during the  
48 decay of root cells and are significant environmental molecules for soil-and plant-interacting bacteria  
49 (6). Although HCAs are generally a strong bacterial repellent, they appear to be chemoattractants in  
50 the case of rhizobia and agrobacteria for which they can be used as trophic resources and/or induced-  
51 virulence molecules (7-11). We have previously showed that HCAs degradation *via* the SpG8-1b region  
52 interferes with virulence genes expression suggesting that this metabolic pathway is important for the  
53 transition between the two lifestyles (rhizospheric versus pathogenic) of *Agrobacterium* (11). Such a  
54 transition requires a fine-tune regulation of gene expression to express the appropriate genes at the  
55 right time (12-14).

56

57 The SpG8-1b genomic region encodes six enzymes (Figure 1A). Five of them operate in this sequential  
58 order for the degradation of ferulic acid leading to different intermediates (5): Atu1416 (a feruloyl-CoA  
59 synthase), Atu1417 (an enoyl-CoA hydratase), Atu1415 (a phenylhydroxypropionyl-CoA  
60 dehydrogenase), Atu1421 (a 4-hydroxy-3-methoxyphenyl- $\beta$ -ketopropionyl-CoA  $\beta$ -keto-thiolase) and  
61 Atu1420 (a tetrahydrofolate-dependent vanillate O-demethylase). Atu1420 shares 56% sequence  
62 identity with *Sphingomonas paucimobilis* and *Sphingobium* sp. SYK-6 homologues of known structures  
63 (PDB 5TL4 (15) and PDB 5X1I (16), respectively). This enzyme degrades vanillic acid into  
64 protocatechuic acid using the tetrahydrofolate (H4F) cofactor and producing the N5-methyl-  
65 tetrahydrofolate compound (MH4F) (5). Protocatechuic acid is then processed by *pca* genes to produce  
66 intermediates of the tricarboxylic acid (TCA) cycle (17). Based on sequence identity of 29% with the  
67 N5,N10-methylene tetrahydrofolate reductase MetF of *Sphingobium* sp. SYK-6, Atu1418 the sixth  
68 enzyme of the SpG8-1b genomic region, is likely a 5,10-methylene tetrahydrofolate reductase which  
69 transforms MH4F into N5,N10-methylenetetrahydrofolate (MEF), which would, in turn, allow the  
70 regeneration of H4F (4,18) (Figure 1A).

71 Although the SpG8-1b genomic region degrades both ferulic and *p*-coumaric acids, this latter induces  
72 the gene expression of the first part of the SpG8-1b region while ferulic acid induces that of the whole  
73 pathway (11). Therefore, two expression units are differently regulated suggesting the existence of two  
74 regulators. These regulators are Atu1419 (predicted to be a GntR member) and Atu1422 denoted HcaR

75 (for hydroxycinnamic acid catabolic repressor belonging to the MarR family), respectively (4,11) (Figure  
76 1B). HcaR is the repressor of its own transcription and that of the first *atu1416* and *atu1417* genes of  
77 HCA degradation pathway (11). However, because *atu1415* and *atu1416* belong to the same  
78 transcription unit as well as *atu1421* and *hcaR* do, HcaR also regulates *atu1415* and *atu1421* genes  
79 expression, totalizing the regulation of five genes (Figure 1B). In contrast to HcaR, the second  
80 regulatory protein Atu1419 likely involved in the second part of the pathway corresponding to the  
81 vanillate degradation remains uncharacterized so far.

82

83 Herein, we investigated the molecular role and structural aspects of Atu1419 combining *in vitro* and *in*  
84 *vivo* approaches. We first proved that Atu1419 was a transcription repressor of three genes of the  
85 second part of the HCA degradation pathway. None of HCA degradation intermediates could release  
86 Atu1419 from DNA binding. Nonetheless, structural analysis of five high-resolution crystal structures of  
87 Atu1419 in apoform, in complex with a fortuitous citrate molecule bound to the effector domain  
88 originated from the crystallization condition (2 structures), in complex with DNA and in complex with  
89 both DNA and citrate, helped us infer a possible effector molecule, which was confirmed by gel shift  
90 assays and microcalorimetry. The structures revealed Atu1419 to be a member of the VanR group of  
91 the FadR C-terminal domain (FCD; Pfam PF07729) subfamily of the large GntR superfamily of  
92 transcriptional factors (>93135 members in Pfam database) (19-22). The FCD subfamily encompasses  
93 two groups of regulators namely FadR and VanR. So far, the dimeric FadR from *Escherichia coli* was  
94 the best characterized of the FadR group of FCD-GntR regulators shown to be regulated by the acyl-  
95 CoA effector and able to bind specific palindromic DNA through a winged Helix-Turn-Helix (wHTH) motif  
96 (23). Like FadR, Atu1419 possesses a characteristic molecular architecture, composed of a conserved  
97 N-terminal DNA binding domain containing the wHTH motif and a C-terminal effector  
98 binding/oligomerization domain. Unlike FadR, this latter domain of Atu1419 displays six helices instead  
99 of seven observed in members of FadR group. Atu1419 is the first example of a transcriptional regulator  
100 of the whole GntR superfamily to be tetrameric. Our work brings new insights into mechanistic aspects  
101 of such repressor, which uses an induced-allosteric mechanism for DNA release upon effector binding.

102

## 103 MATERIAL AND METHODS

### 104 Bacterial strains and growth conditions

105 The bacteria and plasmids used for this study are listed in Supplementary Table S1. *Escherichia coli*  
106 were grown routinely, with shaking (150 rpm), at 37°C in LB medium. Growth media were supplemented  
107 with appropriate antibiotics (tetracycline, 10 µg/ml; gentamicin, 15 µg/ml; ampicillin, 100 µg/ml) when  
108 necessary. The *A. fabrum* strains were grown with shaking (160 rpm), at 28°C in YPG (Yeast Peptone  
109 Glucose)-rich medium or in AT minimal medium supplemented with 10 mM succinate and 10 mM  
110 ammonium sulfate. AT minimal medium was supplemented with 750 µM of ferulic acid or citrate and  
111 with the appropriate antibiotic (gentamicin, 10 µg/ml). Ferulic acid and MH4F were obtained from Sigma  
112 Aldrich (St. Louis, USA) and MEF from Merck Company (Switzerland).

113

### 114 Construction of the deletion mutant C58 $\Delta$ *atu1419* and transcriptional fusions

115 The C58 $\Delta$ *atu1419* and C58 $\Delta$ *atu1420* strains were constructed according to a strategy as described  
116 (4,11). Vectors containing the recombinant region (amplified by PCR with specific primers listed in  
117 Supplementary Table S2), flanking downstream and upstream of the *atu1419* or *atu1420* genes, were  
118 introduced into *A. fabrum* C58 by electroporation. Single-crossover integration was selected by  
119 gentamycin resistance on YPG medium plates. Gentamycin-resistant colonies were spread on YPG  
120 plates containing 5% of sucrose to obtain plasmid excision and double-crossover events leading to  
121 nonpolar mutants. *atu1419* and *atu1420* deletions were confirmed by PCR analysis and DNA  
122 sequencing (GenoScreen, Lille, France).

123 pOT1e (24) transcriptional fusions of the promoter regions of SpG8-1b genes, namely *Patu1419* and  
124 *Patu1420* were generated as described (11) (Supplementary Table S2 for specific primers). Reporter  
125 constructions were introduced into *A. fabrum* C58 wild-type and derivatives by electroporation, and  
126 gentamycin-resistant colonies were selected.

### 127 Measurement of promoter activity

128 Genes expression was measured after 24 hours in *A. fabrum* with a pOT1e plasmid harboring an eGFP  
129 transcriptional fusion (24) as described (11). Results were normalized by dividing the fluorescence level  
130 by the optical density at 600 nm values. At least five technical replicates and two biological replicates  
131 were performed for each condition. Differences between conditions were determined with Tukey test  
132 (P-value= 0.05).

### 133 Oligonucleotides and DNA preparation

134 The synthetic palindromic oligodeoxyribonucleotide 5'-ATGTATACAT-3' was purchased from Sigma-  
135 Aldrich (Darmstadt, Germany). Oligonucleotide solution in sterile water at 2 mM was hybridized by

136 heating to 90°C for 5 min and cooling in the crystallization room at 18°C overnight to produce a 10-mer  
137 DNA.

138 The *atu1420* promoter regions were amplified with specific primer pairs listed in Supplementary Table  
139 S2. The *atu1416-1417*, *atu1418-1419*, *virB* and *hcaR* promoter regions were prepared as previously  
140 described (11) and purified with a PCR Clean-up kit (Macherey-Nagel, Düren, Germany).

#### 141 **Cloning, expression and purification of Atu1419 and Atu1419-H3A mutant**

142 Coding sequences for Atu1419 was amplified by PCR adding a C-terminal 6-Histidine tag and using  
143 *atu1419F* and *atu1419R* primers and was inserted into the NdeI/XhoI restriction sites of the pET-20b  
144 vector (Novagen, Merck Biosciences, France). The nucleotide sequence was confirmed by DNA-  
145 sequence analysis (GATC Biotech, Mulhouse, France). *E. coli* BL21 competent cells transformed with  
146 pET-20b-Atu1419 were grown in LB media until OD<sub>600</sub> of 0.8 and protein production was induced by  
147 0.5 mM isopropyl β-D-thio-galactopyranoside (IPTG) for 3h at 37°C. Cells were centrifuged at 4000 g  
148 for 15 min at 4°C, resuspended in a buffer of 50 mM Tris-HCl pH 8, 300 mM NaCl and 20 mM imidazole  
149 and disrupted by sonication. After centrifugation at 25000 g for 30 min at 4°C, the filtrated supernatant  
150 was loaded onto a 5 ml His-Trap HP column (GE Healthcare, Chicago, Illinois, USA). After a washing  
151 step of 6% with 50 mM Tris-HCl pH 8, 300 mM NaCl and 300 mM imidazole (Buffer B), protein elution  
152 was performed with Buffer B. Protein fractions were loaded onto a gel filtration column (HiLoad 26/60  
153 Superdex 200 prep grade, GE Healthcare) equilibrated with 50 mM Tris-HCl pH 8 and 150 mM NaCl.  
154 The protein fractions were pooled, concentrated and stored at -80°C.

155 The synthetic gene (Genscript, Piscataway, New Jersey, USA) coding for Atu1419 mutant (H192A,  
156 H141A and H214A) namely Atu1419-H3A was inserted into pET-20b. The Atu1419-H3A mutant was  
157 expressed and purified as the wild-type protein described above.

158 **Size exclusion chromatography (SEC) and SEC-MALS.** For size exclusion chromatography (SEC)  
159 and SEC coupled to multi-angle light scattering (SEC-MALS) analyses, apo Atu1419 was prepared at  
160 25 μM and Atu1419 in complex with the palindromic DNA was prepared with a ratio protein:DNA of 1:2  
161 in a buffer containing 50 mM Tris pH 8 and 150 mM NaCl. The same buffer was used as the mobile  
162 phase for SEC using a Superdex 200 10/300 GL column on an AKTA FPLC system (GE Healthcare)  
163 and on a Shimadzu HPLC. Multiangle light scattering was detected with a MiniDAWN TREOS light  
164 scattering module and a refractometer Optilab T-rEX (Wyatt Technology).

#### 165 **Electrophoretic mobility shift assay (EMSA)**

166 Atu1419 or Atu1419-H3A mutant were mixed with different promoter regions (*Patu1416-1417*,  
167 *Patu1418-1419*, *PhcaR*, *Patu1420* and *PvirB*) and with variants of the *atu1418-1419* and *atu1420*  
168 regions. The intergenic regions of *virB* was used as a nonspecific control probe. Gel-shift assays were  
169 performed in 10 μl reaction mixture containing 30 nM of DNA probe without and with Atu1419 at different  
170 concentrations in 50 mM Tris-HCl pH 8 and 150 mM NaCl. 50 to 300 μM of MEF, MH4F, H4F or citrate

171 were added for testing their influence on Atu1419-DNA complex formation. After incubation for 30 min  
172 at room temperature, the samples were separated by electrophoresis in TBE buffer (45 mM Tris-HCl  
173 pH 8, 45 mM boric acid and 1 mM EDTA) on non-denaturing 6% or 12% polyacrylamide gels at 150 V  
174 and 4°C for 2 h. Gels were then stained with either SYBR® Green EMSA nucleic acid gel stain  
175 (Invitrogen, Carlsbad, CA, USA) or ethidium bromide for 20 min. DNA was visualized under UV light  
176 (Fisher Bioblock Scientific, Illkirch, France or UVP BioDoc-it2 Imager, Analytic Jena, Germany).

177

## 178 **Crystallization and structure determination of Atu1419**

179 Crystallization conditions are summarized in Table 1. For all protein samples (140 µM tetrameric protein  
180 alone or in complex with 700 µM palindromic DNA), conditions were screened using QIAGEN kits  
181 (Valencia, CA, USA) with a Mosquito nanodrop robot (TTP Labtech, Melbourn, Great Britain) and were  
182 manually optimized at 20°C in hanging drop by mixing equal volumes of the protein or protein-DNA  
183 solution with precipitant solution. Crystals were transferred to a cryoprotectant solution (paraffin oil or  
184 mother liquor supplemented with 20% PEG 400) and flash-frozen in liquid nitrogen. Diffraction data  
185 were collected at 100 K on PROXIMA 1 and PROXIMA 2 beamlines at synchrotron SOLEIL (Saint-  
186 Aubin, France). Intensities were integrated using the XDS package (25) (Table 1).

187 The first structure of Atu1419 in  $P2_12_12_1$  space group was determined at 2.35 Å resolution by single-  
188 wavelength anomalous dispersion (SAD) method at the peak absorption energy of Zinc (Table 1). The  
189 presence of a zinc metal in crystals was found thanks to an X-ray fluorescence emission scan on the  
190 beamline. The steps of zinc ion substructure determination, phases calculation and density modification  
191 were performed using CRANK from CCP4 (Collaborative Computational Project, Number 4) and a  
192 partial model was built using BUCCANEER (CCP4). This model was then used to calculate the phases  
193 of a higher resolution dataset at 2 Å resolution leading to the complete polypeptide chain model. A  
194 tetramer is present in the asymmetric unit. Other structure determinations were performed by molecular  
195 replacement with PHASER (26) using the first refined structure of Atu1419 (monomer, dimer or  
196 tetramer). Because of the anisotropy of the diffraction of Atu1419-DNA complex in  $P6_422$  crystals and  
197 apo Atu1419, the DEBYE and STARANISO programs developed by Global phasing Ltd were applied  
198 to the data scaled with XDS using the STARANISO server (<http://staraniso.globalphasing.org/>). These  
199 programs perform an anisotropic cut-off of merge intensity data on the basis of an analysis of local  $I/\sigma(I)$ ,  
200 compute Bayesian estimates of structures amplitudes, taking into account their anisotropic fall-off, and  
201 apply an anisotropic correction to the data. The corrected anisotropic amplitudes were used for further  
202 refinement. Refinement of each structure was performed with BUSTER-2.10 (27) employing TLS  
203 groups and NCS restraints. Inspection of the density maps and manual rebuilding were performed using  
204 COOT (28). Refinement details of each structure are shown in Table 1. Molecular graphics images were  
205 generated using PyMOL (<http://www.pymol.org>).

## 206 **Circular dichroism experiments (CD)**

207 Circular dichroism in the far-UV region was performed using a spectropolarimeter (Jasco J-810, Jasco,  
208 Lisses, France) equipped with a water-cooled Peltier unit (Jasco circular dichroism spectrometer model  
209 J810). Apo Atu1419 and Atu1419-H3A mutant were both concentrated at 25  $\mu\text{M}$  in 50 mM Tris pH 8  
210 and 150 mM NaCl. Spectra were recorded in a cell width of 0.1 mm path length (121.QS, Hellma, Hellma  
211 Analytics, Müllheim, Baden Württemberg, Germany) from 190 to 240 nm at 20°C. Five consecutive  
212 scans from each sample were merged to produce an averaged spectrum; the spectra were corrected  
213 using buffer baselines measured under the same conditions. Data were recorded in mdeg and  
214 converted using the mean residues ellipticity method ( $\text{deg}\cdot\text{cm}^2\cdot\text{mol}^{-1}$ ). Secondary structure estimates  
215 were derived from the normalized spectra using the CDSSTR, SELCON3, CONTIN of the DICHROWEB  
216 server (29,30).

### 217 **Differential scanning calorimetry (auto PEAQ DSC)**

218 Thermal stability of 10  $\mu\text{M}$  apo Atu1419, 10  $\mu\text{M}$  Atu1419 in the presence of 100  $\mu\text{M}$  MEF and 20  $\mu\text{M}$   
219 Atu1419-H3A mutant was performed by DSC on an auto PEAQ DSC (Malvern, France) in a standard  
220 buffer. Each measurement was preceded by a baseline scan with the standard buffer. Scans were  
221 performed at 1  $\text{K}\cdot\text{min}^{-1}$  between 20 and 90°C. The heat capacity of the buffer was subtracted from that  
222 of the protein sample before analysis. Thermodynamic parameters were determined by fitting the data  
223 to the following equation:

$$224 \quad \Delta C_p(T) = \frac{K_d(T) \Delta H_{cal} \Delta H_{vH}}{[1 + K_d(T)]^2 RT^2}$$

225 where  $K_d$  is the equilibrium constant for a two-state process,  $\Delta H_{vH}$  is the enthalpy calculated on the  
226 basis of a two-state process and  $\Delta H_{cal}$  is the measured enthalpy.

### 227 **Isothermal titration microcalorimetry measurements (ITC)**

228 Isothermal titration microcalorimetry experiments were performed with an ITC200 isothermal titration  
229 calorimeter from MicroCal (Malvern, Orsay, France). The experiments were carried out at 20°C. Protein  
230 concentration in the microcalorimeter cell (0.2 ml) was 100  $\mu\text{M}$ . Nineteen injections of 2  $\mu\text{l}$  MEF solution  
231 at 1.2 mM were performed at intervals of 180 s while stirring at 500 rpm. The experimental data were  
232 fitted to theoretical titration curves with software supplied by MicroCal (ORIGIN®).

### 233 **Electron Microscopy**

234 Atu1419 (150 nM) was incubated with equimolar *Patu1418-1419* region (370 bp containing two  
235 palindromes separated by 190 bp) for 10 min at room temperature in a buffer containing 50 mM Tris pH  
236 8 and 150 mM NaCl. Samples were deposited on a glow-discharged carbon coated grid and stained  
237 with 2% uranyl acetate. Images were recorded with a Lab6 Tecnai Spirit operating at 80kV and a  
238 Quemesa Olympus CCD camera. Nominal magnification was X 45 000 corresponding to 3.17 Å/pixel.

239

## 240 RESULTS AND DISCUSSION

### 241 The transcriptional regulator *Atu1419* is the second repressor of the HCAs degradation pathway

242 To study the role of *Atu1419* in transcriptional regulation of the HCAs degradation genes, we  
243 constructed reported fusions with pOT1e plasmids containing each promoter region of the SpG8-1b  
244 region (Figure 1) cloned upstream the *egfp* gene. This allowed reporting the transcription of each gene  
245 by measuring the eGFP fluorescence. The *atu1419* and *atu1420* plasmid reporter gene fusions were  
246 constructed in this study. Those corresponding to *atu1416* and *atu1418* were already available (11).  
247 The plasmid reporter fusions were introduced into the wild-type *A. fabrum* C58 strain to evaluate gene  
248 expression in response to ferulic acid. Compared to the fluorescence level measured in the absence of  
249 ferulic acid, the fluorescence level measured in the presence of ferulic acid was higher for the four  
250 reporter fusions (Table 2). Hence, *atu1416*, *atu1418*, *atu1419* and *atu1420* genes were induced in the  
251 presence of ferulic acid. The four plasmid reporter fusions were also introduced into the *C58Δatu1419*  
252 mutant strain to compare genes expression with that of the wild-type C58 strain in the absence of ferulic  
253 acid. The fluorescence level measured after 24 hours for *atu1418*, *atu1419* and *atu1420* reporter  
254 fusions were respectively 3.67, 3.92 and 1.58 times higher in the *C58Δatu1419* mutant strain than in  
255 the wild-type strain (Table 2). Thus, in the strain lacking *Atu1419* regulatory protein (*C58Δatu1419*), the  
256 reporter fusions for *atu1418*, *atu1419* and *atu1420* genes were constitutively expressed. In contrast,  
257 the fold change between *C58Δatu1419* and the wild type strains was 0.63 and 0.97 for the *atu1416*  
258 gene fusion and the empty pOT1e vector, respectively indicating that *atu1416* gene expression was not  
259 repressed by *Atu1419* (Table 2). These results showed that *Atu1419* was a transcriptional repressor  
260 that regulates *atu1418*, *atu1420*, and its own transcription.

### 261 DNA-binding targets

262 To characterize the target DNA sequence of *Atu1419*, we purified *Atu1419* (theoretical molecular weight  
263 of ~26 542 Da for a monomer), which appeared as a tetramer in solution according to gel filtration/SEC-  
264 MALS chromatography (Supplementary Figure S1). Using the intergenic regions (between 300 and  
265 400-base pair (bp)) of *atu1416-1417*, *atu1418-1419*, *atu1420*, *hcaR* and *virB* (negative control gene  
266 outside the SpG8-1b region) as DNA probes for binding assays (Figure 2A), we showed that *Atu1419*  
267 bound to the *atu1418-1419* and *atu1420* promoter regions only, in agreement with the gene expression  
268 data described above.

269 In silico comparison of the promoter regions of *atu1418-1419* and *atu1420* using BPROM program (31)  
270 revealed three 10-mer identical palindromic sequences (5'-ATGTATACAT-3'), two in *atu1418-1419*  
271 promoter region and one in *atu1420* promoter region (Figure 2B). A palindromic sequence overlaps the  
272 -10 box regulatory element of *atu1418* and *atu1420*, whereas in the *atu1418-1419* promoter sequence,  
273 an additional palindromic sequence is found between the -10 and the -35 regulatory elements of the  
274 *atu1419* (Figure 2B). Using electrophoretic mobility shift assay (EMSA), we showed that *Atu1419* was  
275 able to bind each palindrome of the *atu1418-1419* promoter sequence without the presence of the other  
276 palindrome meaning that only one palindrome site was required for binding (Figure 2C). Nonetheless,

277 the intensity of the shifted bands was greater for the DNA fragment containing both palindromes (Figure  
278 2C). We also analyzed the quaternary structure of Atu1419 in complex with the 10-bp palindrome using  
279 gel filtration/SEC-MALS measurements (Supplementary Figure S1). Atu1419 was also tetrameric upon  
280 DNA binding.

### 281 **Crystal structures of Atu1419 in complex with a fortuitous ligand**

282 We solved the first structure of Atu1419 from crystals grown in sodium citrate buffer using SAD method  
283 at the peak absorption energy of Zinc at 2 Å resolution in the space group  $P2_12_12_1$  (Table 1). The zinc  
284 ion comes from *E. coli* protein expression because no metal was added during protein purification and  
285 crystallization. Four molecules (A, B, C and D) are present in the asymmetric unit and form a tetramer  
286 (a dimer of dimer) (Figure 3A), which is consistent with the observation that Atu1419 is a tetramer in  
287 solution (Supplementary Figure S1). Each monomer consists of an N-terminal DNA binding domain  
288 (residues 1-71) and a C-terminal all  $\alpha$ -helical effector binding domain (residues 76-244) (Figure 3B).  
289 The DNA binding domain is composed of three helices ( $\alpha 1$ - $\alpha 3$ ) with helix  $\alpha 2$  and helix  $\alpha 3$  forming the  
290 helix-turn-helix motif and two anti-parallel  $\beta$ -strands ( $\beta 1$ - $\beta 2$ ) connected by a small loop designated as  
291 the wing motif. The secondary element with six helices ( $\alpha 4$ - $\alpha 9$ ) and topology of the C-terminal domain  
292 place Atu1419 in the VanR group of the FCD subfamily of GntR transcriptional regulators.  
293 Approximately 2776 Å<sup>2</sup> of accessible surface area is buried upon dimerization for dimers AB or CD  
294 corresponding to an average of 11.7% of the total surface area of each monomer and 41 amino acids  
295 per monomer. The interface between dimers AB and CD involves side chains of both domains: helix  $\alpha 3$   
296 and strand  $\beta 1$  (residues 49-67) of the DNA binding domain and the three helices  $\alpha 4$  (residues 78-100),  
297  $\alpha 7$  (residues 150-163) and  $\alpha 9$  (residues 208 and 212) of the effector binding domain (Figure 3B). Arg72  
298 in the linker region participates to the dimer interface. Two salt bridges with Glu57-Arg63' (the prime  
299 refers to the second monomer in the dimer), and two polar interactions Glu57-Ser53' and Asn62-Arg155'  
300 are located in the N-terminal domain whereas fourteen H-bonds/salt-bridges including Asp81, Glu84,  
301 Arg95, Arg100, Ser150, Arg155, Glu156, Glu208 and Arg212 belong to the C-terminal domain. The  
302 contacts of dimer AD through eleven polar interactions/salt bridges bury 686 Å<sup>2</sup> per subunit and concern  
303 23 amino acids, which are located in the loop between helices  $\alpha 5$ - $\alpha 6$  (mainly residues 123-125), helices  
304  $\alpha 8$  (residues 183-194) and  $\alpha 9$  (residues 203-216) (Figure 3B). The dimer BC displays a smaller  
305 interface of 557 Å<sup>2</sup> per subunit comprising 21 amino acids and the same structural elements as for  
306 dimer AD. The total surface contact area between two neighbouring subunits within the tetramer is  
307 characteristic of biological interactions (32).

308 Remarkably, the four subunits within the tetramer are not identical: molecule A shows large  
309 conformational changes as indicated by an average root mean square deviation (RMSD) of 1.28 Å for  
310 all C $\alpha$  atoms compared with the subunits B/C/D, which are more similar (average RMSD of 0.7 Å for all  
311 C $\alpha$  atoms). This is due to the presence of a citrate originated from the crystallization condition, which  
312 binds molecule A in the effector binding site in a different orientation (orientation A; Figures 3C and 3D)  
313 than that for citrates in subunits B/C/D (orientation B; Figures 3C and 3E), which bind similarly (Figure

314 3C). Four loop regions (shown in red in Figure 3C), comprised of residues 64-67 of the wing between  
315  $\beta 1$  and  $\beta 2$  of the wHTH motif, residues 119-130 between helices  $\alpha 5$  and  $\alpha 6$ , residues 169-184 between  
316 helices  $\alpha 7$  and  $\alpha 8$  and residues 225-244 corresponding to the end of the effector binding domain, can  
317 move between 3 and 10 Å. The loop region 169-184 can drastically rearrange upon ligand binding. In  
318 molecule A, the  $C\alpha$  atoms of Ser169, Lys175 and Arg183 are respectively, 0.92 Å, 6.84 Å and 7.34 Å  
319 away from those in molecules B/C/D, allowing the side chains of Lys175, Arg183 and the NH main  
320 chain of Ser169 to interact with the citrate molecule (Figures 3C and 3D). These latter protein-citrate  
321 interactions cannot exist in subunits B/C/D. Nonetheless, all bound citrates share interactions with  
322 Arg86, Tyr133, Asn137, His141, His214, Asn221 and a  $Zn^{2+}$  ion that co-purified with Atu1419 (Figures  
323 3D and 3E). Thirteen polar interactions are observed between monomer A and the citrate molecule  
324 (orientation A), which is buried within the monomer, leaving only 26.6 Å<sup>2</sup> or 8.4% of the molecule surface  
325 exposed to solvent. In contrast, there are only ten polar interactions between monomers B/C/D and the  
326 citrate with a similar buried surface area.

327 The orientation B of the citrate was also observed in another structure of Atu1419 solved at a higher  
328 resolution of 1.75 Å but in a different space group ( $P2_12_12$ ). Here, two similar monomers (RMSD of 0.98  
329 Å for all  $C\alpha$  atoms) are in the asymmetric unit and form a dimer, which in turn form a tetramer by the  
330 crystal symmetry with globally unchanged dimer interfaces (1553 Å<sup>2</sup> and 701 Å<sup>2</sup> per subunit for dimers  
331 AB and AD, respectively) compared with those from the  $P2_12_12_1$  structure. They resemble subunits  
332 B/C/D of the  $P2_12_12_1$  structure and bind similarly a citrate molecule. Nonetheless, their citrates are  
333 slightly shifted by 0.6 Å towards Arg86 losing the interaction with Asn221 compared with those in the  
334  $P2_12_12_1$  structure (Supplementary Figure S2).

### 335 **Crystal structures of Atu1419 in complex with the palindromic DNA**

336 The structures of two palindromic DNA-Atu1419 complexes solved at 2.79 Å resolution ( $P6_422$  space  
337 group) and 2.05 Å resolution ( $C222_1$  space group) present a distinct neighboring crystal packing with  
338 an asymmetric unit containing a monomer bound to a single DNA strand and a dimer bound to the 10-  
339 mer palindromic DNA, respectively (Table 1, Supplementary Figure S3). Nonetheless, a tetramer,  
340 where dimers AB and CD bind each to a DNA palindrome, was reconstituted by crystal symmetries  
341 (Figures 4A and 4B) in line with the conservation of Atu1419 tetramer in solution upon DNA binding.  
342 The three monomers of the asymmetric units (one in  $P6_422$  and two in  $C222_1$ ) are similar with an  
343 average RMSD value of 1 Å for all  $C\alpha$  atoms making almost identical interactions with DNA, although  
344 the positions of the DNA binding domains within the dimers between the two crystal structures do not  
345 completely overlap (Figure 4C). This observation explains the different crystal packing resulting of  
346 flexibility from both the DNA ligand and the DNA binding domains of Atu1419. Each monomer  
347 recognizes a half-site DNA with helices  $\alpha 2$  and  $\alpha 3$  of the HTH motif making nine polar interactions with  
348 both strands in the major groove of the DNA (Figures 4D and 4E). Helix  $\alpha 3$  via Ser44, Thr46, Arg45  
349 and Arg49 side chains is responsible for six hydrogen bonds with both strands, half with oxygens of  
350 phosphate groups 5' of guanine (G3) at position 3 on one strand and of adenine (A5) at position 5 on

351 the complementary strand. The other half is made by the guanidinium group of Arg45, which provides  
352 specific contacts with the N7 and O6 atoms of G3 on one strand and by OG1 of Thr46 with the N7 of  
353 A5 on the other strand (Figure 4C). The remaining H-bonds come from helix  $\alpha 2$  via the Arg31 side chain  
354 and the main chain amino group of Glu34, and an additional interaction is present with the main chain  
355 NH of His9 in helix  $\alpha 1$ . They consist of phosphate contacts with A1 and T2 on one DNA strand and T4  
356 on the other.

357 All Atu1419-DNA subunits contain a bound  $Zn^{2+}$  ion at the same position as that observed in both  
358 Atu1419-citrate complexes. In contrast to the protein-DNA complex in  $C222_1$  space group, which  
359 crystallized in MES buffer, the  $P6_422$  protein-DNA complex reveals a bound citrate in the effector  
360 binding pocket. This citrate adopts the orientation B described in both Atu1419-citrate complexes,  
361 except for molecule A (orientation A) in the  $P2_12_12_1$  structure. Because both tetrameric Atu1419-DNA  
362 structures are similar, the presence of the bound citrate in orientation B in all subunits of one DNA  
363 complex has clearly no effect on Atu1419 for DNA binding and DNA release, in agreement with EMSA  
364 assay (Figure 4G) and promoter activity (Table S3).

365 We modified the specifically recognized guanine base G3 by an adenine base and its partner base C8  
366 by a thymine on each strand within the unique palindrome of the *atu1420* promoter region. Gel-shift  
367 assays showed that Atu1419 was no longer able to bind *Patu1420s* AT mutant (Figure 4F). Therefore,  
368 the guanine at position 3 has an essential role in the DNA palindrome binding by Atu1419 meaning that  
369 Arg45 has a key role in recognizing this guanine base.

### 370 **Crystal structure of apo Atu1419 and structural comparison**

371 We solved the structure of Atu1419 in the apoform at 2.7 Å resolution using Tris-HCl buffer instead of  
372 citrate buffer in the crystallization condition to avoid any bound citrate (Table 1). The asymmetric unit  
373 contains a tetramer with a bound  $Zn^{2+}$  ion in each effector binding domain. Asn137 and three histidine  
374 (His141, His192 and His214) side chains form the metal binding site of Atu1419 and chelate the zinc  
375 ion with a classical tetrahedral coordination geometry and average distances around 2.2 Å (Figure 5A).  
376 We mutated the three histidine (His141, His192 and His214) into alanine to make the triple point mutant  
377 Atu1419-H3A and alter the metal binding site. The zinc ion holds helices  $\alpha 6$ ,  $\alpha 8$  and  $\alpha 9$  involved in the  
378 tetrameric interface far from the DNA binding domain, and likely interacts with the effector as shown by  
379 the structures solved with a citrate taking the place of the effector. Atu1419-H3A is correctly folded as  
380 checked by using circular dichroism (Supplementary Figure S4) and shares the same secondary  
381 structure content (about 58%  $\alpha$ -helices and 1%  $\beta$ -sheets) as the wild-type protein in line with what is  
382 observed in all crystal structures of Atu1419. Similar to the wild-type protein, this mutant is tetrameric  
383 and capable of binding *atu1418-1419* and *atu1420* promoter regions.

384 The dimeric (dimers AB/CD) and tetrameric interfaces (dimers AD/BC) covering around 1400 Å<sup>2</sup> and  
385 516 Å<sup>2</sup> per subunit, respectively, are comparable to those of Atu1419-citrate complexes and Atu1419-  
386 DNA complexes. Subunits A and D overlap well (RMSD of 0.53 Å), as well as subunits B and C (RMSD

387 of 0.83 Å), whereas subunits A and B or C and D show a RMSD over 2 Å, mainly due to differences in  
388 the position of their HTH motif and the end of their C-terminal domain, evidencing large flexibility  
389 (Supplementary Figure S5A). This is confirmed by the structural comparison of the DNA binding  
390 domains of the apo dimer AB with those of the Atu1419-DNA complex (Figure 5B). While subunits A  
391 are rather similar, helix  $\alpha$ 3 of the apoform subunit B clashes into the DNA sugar-phosphate backbone.  
392 Indeed, this helix is far from its optimized position for DNA binding, which is perpendicular to the helical  
393 axis of the DNA. A displacement up to 7 Å would be required to correctly places its wHTH motif. A  
394 similar structural analysis between the DNA binding domains of the Atu1419-citrate complexes and  
395 Atu1419-DNA complexes led to similar conclusions (Supplementary Figures S5B-D).

396 It is noteworthy that the conformation of the effector binding pocket in all subunits bound or not to DNA  
397 and containing a citrate in orientation B is similar to that of the empty pocket observed in the apo form  
398 and one DNA complex. This suggests that this citrate may mimic a non-productive-like binding in the  
399 effector binding site.

400

#### 401 **Comparison with other FCD members**

402 Atu1419 belongs to the VanR subgroup of the FCD subfamily of the large GntR superfamily due to the  
403 number of helices in its effector binding domain. The FCD subfamily is divided into two groups; VanR  
404 and FadR. Members that are structurally characterized in FadR subgroup possess an additional helix  
405 after the linker region at the beginning of the effector binding domain (23,33-35). This major difference  
406 leads to a domain-swapped quaternary structure, in which the DNA binding domain of FadR subunit A  
407 crosses the dimerization interface to be in contact with the effector binding domain of subunit B (35-37).  
408 This is not observed in the VanR subgroup where both domains from the same subunit are associated.

409 Atu1419 is now the seventh VanR member to be structurally characterized. The six others are  
410 *Thermotoga maritima* TM0439 (PDBs 3SXY/3FMS (38)), *Ralstonia eutropha* JMP134 YP\_298823.1  
411 (PDB 3IHU no related publication), *Pseudomonas syringae* PS5454 (PDB 3C7J, no related publication),  
412 *Rhodococcus* sp. *RHA1* (PDB 2HS5, no related publication), *Escherichia coli* McbR/YncC (PDB 4P9F  
413 (37)) and *Listeria monocytogenes* MouR (PDB 6EP3 (39)). Structural comparison using SSM-EBI  
414 (<http://www.ebi.ac.uk/msd-srv/ssm>) reports RMSD of 3.19 Å over 190 C $\alpha$  atoms/3.46 Å over 184 C $\alpha$   
415 atoms between the full-length of Atu1419 and MouR (PDB 6EP3)/TM0439 (PDB 3SXY), respectively.  
416 The same search using the C-terminal domain of Atu1419 only improves the RMSD values to 2.59 Å  
417 and 2.71 Å over 127 residues with the effector binding domains of TM0439 and MouR corresponding  
418 to 15% and 13% sequence identity, respectively (Supplementary Figure S6A). The best match concerns  
419 the effector binding domain of McbR/YncC (PDB 4P9F) with a RMSD of 2.23 Å over 132 residues and  
420 18% sequence identity, meaning that there are major significant differences between Atu1419 and the  
421 six other VanR members. While only the C-terminal domain is responsible for dimerization for most  
422 VanR regulators (37), Atu1419 is similar to McbR/YncC in using both the N- and C-terminal domains

423 as the dimeric interface. However, the dimer of Atu1419 does not structurally resemble that of  
424 McbR/YncC (Supplementary Figure S6B).

425 Like Atu1419, two other VanR members, which are TM0439 and PS5454 display a metal binding site  
426 with three histidine residues and an asparagine or an aspartate residue involved in the metal  
427 coordination (37,38). These histidine residues are conserved and structurally close (Supplementary  
428 Figure S6C). LldR (PDB 2DI3) from the FadR group binds a zinc ion chelated by these three conserved  
429 histidines and an aspartate (35). It was proposed that an additional subgroup within the FCD subfamily  
430 could be created for regulators from both FadR and VanR members, which are capable of binding to  
431 metal ions (35,38). Using thermal denaturation experiments by differential scanning calorimetry (DSC),  
432  $T_m$  of 52.6°C and 34°C were measured with the wild-type Atu1419 and Atu1419-H3A mutant  
433 respectively (Supplementary Figure S7). The drastic difference of almost 20°C indicates that the metal  
434 assists in stabilizing the structure affording an explanation as to why Atu1419-H3A could not be  
435 concentrated over 50  $\mu$ M without precipitating, in contrast to the wild-type protein (140  $\mu$ M). All attempts  
436 to crystallize Atu1419-H3A were unsuccessful.

437 Atu1419 is the first VanR member to be structurally characterized in complex with DNA whereas several  
438 FadR-DNA complexes are available (23,33,34). Each dimer of Atu1419 within the tetramer can bind an  
439 identical palindrome. Similarly to regulators with a WHTH motif such as MarR regulators (40,41), FCD  
440 regulators bind to one half-site of the palindromic DNA, with the dimerization interface helping to  
441 establish the spacing between the two half-sites. The DNA binding domains of Atu1419, which are  
442 involved in the dimerization interface, allow Atu1419 to bind a short palindrome of 10 base pairs. As in  
443 *E. coli* FadR (PDB 1H9T (23) and 1HW2 (33)) and in *Vibrio cholerae* FadR (PDB 4P9U(34)), the DNA-  
444 binding site of each Atu1419 monomer is recognized by conserved residues such as Glu34 in helix  $\alpha$ 2,  
445 Arg45 (specific DNA contacts), Thr46 and Arg49 (phosphate backbone contacts) in helix  $\alpha$ 3 that interact  
446 with the major groove and Gly66 in the tip of the wing (residues 64-68) between  $\beta$ 1 and  $\beta$ 2. Nonetheless,  
447 the wing is not crucial for DNA interaction of Atu1419 unlike FadR, which recognizes a pseudo-  
448 palindrome of 17 base pairs. Indeed, His65, which specifically recognizes a DNA base in FadR is a  
449 glycine in Atu1419. DNA binding domains superposition of the Atu1419-DNA complex with those of *E.*  
450 *coli* and *V. cholerae* FadR-DNA complexes shows that although the positions of subunits A are rather  
451 similar, the second subunit of Atu1419 makes steric clashes with the DNA bound to FadR and that of  
452 FadR is too far from the DNA bound to Atu1419 (Supplementary Figure S8). Atu1419 displays only one  
453 specific interaction shared in FadR with the guanine present within the major groove of DNA *via* their  
454 conserved Arg45, a typical feature of the GntR family (22). The other specific DNA contacts of FadR  
455 (*via* Arg35, Thr44, Thr46 and His65) are not comparable with those of Atu1419. The recognized DNA  
456 sequence of Atu1419 which is 5'-ATGTATACAT-3' is in agreement with the predicted DNA signature  
457 for the GntR family: 5'-(N)<sub>y</sub>GT(N)<sub>x</sub>AC(N)<sub>y</sub>-3' where the number x and y vary (20). Later, this DNA binding  
458 signature was suggested to be modified as 5'-TNG(N)<sub>n</sub>CNA-3' on the basis of base-specific interactions  
459 (22) or as 5'-TGGTN<sub>x</sub>ACCA-3' for FadR subgroup (35) but both sequences are not appropriate for  
460 Atu1419.

461 The DNA binding of Atu1419 requires conformational changes of the DNA binding domains. Indeed,  
462 the distance between the two DNA recognition helices (Thr46 of helix  $\alpha_3$ ) narrows from 12 Å in the  
463 apoform to 9.3 Å in the Atu1419-DNA complex, for a productive interaction with DNA (Figure 5C). A  
464 similar observation was reported for *Vibrio cholerae* FadR (PDB 4P9U (34)). The structures of FadR  
465 repressors in complex with their effector show significant conformational changes transmitted from the  
466 effector binding domain to the DNA binding domain, leading to a conformational state that is no longer  
467 favorable for interaction with DNA (22,23,34). The fundamental process wherein the binding of a ligand  
468 or effector molecule alters the activity of the protein at a distant site is defined as an allosteric  
469 mechanism. In the case of Atu1419, the citrate in orientation A bound in the effector binding pocket  
470 induces large conformational changes from the C-terminal domain to the N-terminal domain. It affects  
471 four different protein regions: the wing of the DNA binding domain and three regions of the effector  
472 binding domain including the C-terminus protein which is in contact with the DNA binding domain  
473 (Figure 3C). The presence of this citrate clearly reveals the plasticity of the effector binding pocket and  
474 the large potential rearrangement of the repressor. It also shows that within the tetramer, one subunit  
475 can adopt a different conformation around the effector binding pocket and further away (Figure 3C)  
476 compared to the three others subunits, highlighting an allosteric mechanism. The orientation A of the  
477 citrate may mimic an active-like position of the physiological effector part bound to the metal ion.

#### 478 **Atu1419 effector is the N5,N10-methylenetetrahydrofolate (MEF)**

479 The effector molecule bound to the members of the GntR superfamily are often related to catabolic  
480 substrates or intermediates of the pathway controlled by the transcription factor (19,20), and several  
481 molecules are produced during the ferulic acid degradation pathways (5). Because the citrate molecule  
482 was able to bind to the effector binding site of Atu1419, we searched for molecules resembling citrate  
483 among those described in the HCA pathway (Figure 1A), and we asked whether the substrate-cofactor  
484 H4F or the product-cofactor M4HF of the O-demethylase Atu1420 enzyme could be a potential effector.  
485 Indeed, citrate compound with three carboxylate groups mimics two carboxylate groups located at one  
486 end of the H4F or MH4F molecules. Alternatively, MEF, the putative product of Atu1418 enzyme, which  
487 possesses the same two carboxylate groups could also be a potential effector of Atu1419.

488 To verify this, *Patu1418*, *Patu1419* and *Patu1420* plasmid reporter gene fusions were introduced into  
489 the *C58 $\Delta$ atu1418* and *C58 $\Delta$ atu1420* mutant strains. For each strain, the fluorescence level was  
490 monitored in the presence or absence of ferulic acid and compared to the wild-type *A. fabrum* C58  
491 (Figures 6A-C). For the *C58 $\Delta$ atu1418* strain, the overproduction of fluorescence observed in the  
492 presence of ferulic acid is significantly lower than that in the wild-type C58 and *C58 $\Delta$ atu1420* strains.  
493 These results indicate that the presence of *atu1418* gene is important for the full induction of *atu1418*,  
494 *atu1419* and *atu1420* genes expression in the presence of ferulic acid. The accumulation of MH4F and  
495 the lack of MEF production in the defective *C58 $\Delta$ atu1418* mutant suggests that MEF could be the  
496 effector of Atu1419. MEF is not stable in aqueous *in vitro* solutions as it enters a rapid reversible  
497 equilibrium into H4F (42,43). Nonetheless, immediately using freshly-made MEF solution for gel-shift  
498 assays, we were able to show that MEF could relieve repression of Atu1419 (Figure 6D) whereas H4F

499 and MH4F had no effect (Figure 6E). In the C58 $\Delta$ *atu1418* mutant, induction of *Patu1418*, *Patu1419* and  
500 *Patu1420* was not totally abolished, probably due to functional redundancy of N5,N10-methylene  
501 tetrahydrofolate reductase activity in *A. fabrum* genome, which allows to keep a basal pool of folate and  
502 intermediates essential for the cell (44).

503 The interaction between MEF and Atu1419 was confirmed by DSC with a  $T_m$  of 63.5°C for Atu1419 in  
504 complex with MEF compared to the  $T_m$  of 52.6°C for the apo Atu1419 (Figure 6F). This was also  
505 confirmed by isothermal titration microcalorimetry (ITC, Figure 6G). Because MEF instability did not  
506 allow a return to the baseline between two injections, we could not rigorously determine a dissociation  
507 constant  $K_D$  value, which is around 20  $\mu$ M. Injection of MEF towards buffer solution was a control of its  
508 instability effect (Figure 6H). No interaction could be observed between MH4F and Atu1419 by DSC  
509 and ITC, in agreement with the results from EMSA assays.

### 510 **Atu1419 tetramer is the biologically active form**

511 We analyzed the quaternary structure of Atu1419 in complex with MEF using gel filtration measurement  
512 (Supplementary Figure S9). Atu1419 remains tetrameric when bound to MEF. Thus, Atu1419 is a  
513 tetramer in its apo form, upon DNA binding or effector binding suggesting that this quaternary structure  
514 is the biologically active form. Both crystal structures of Atu1419 in complex with DNA revealed that  
515 each dimer of Atu1419 within the tetramer can bind a palindromic site of 10 bp, separated by  
516 approximately 10 nM (Figure 3A). This separation distance is compatible with DNA loop formation  
517 allowing the simultaneous binding of two distant palindromes (190 bp apart) within the intergenic region  
518 of *atu1418-1419*. Thus, Atu1419 tetramer could repress gene expression *via* DNA looping, such as  
519 several negative regulators in prokaryotes (47) with the example of the intensively studied tetrameric  
520 *lac* operon repressor (48).

521 We searched for a second potential DNA binding site of Atu1419 in *atu1420* region and found a  
522 degenerated palindrome (8 bp conserved over the 10 bp palindrome; Figure 7A). The degenerated  
523 palindrome is separated by 109 bp from the palindrome and is located downstream within the open  
524 reading frame of *atu1420* gene (Figure 7A). We then performed EMSA assays with three  
525 oligonucleotides containing either the palindrome, the degenerated palindrome, or both and identified  
526 in the gel a retarded band for each oligonucleotide proving the formation of a stable non-covalent  
527 protein-DNA complex (Figure 7B). Thus, the repressor can recognize a palindrome and a degenerated  
528 palindrome providing it the opportunity to bind simultaneously to two DNA sites in each region (*atu1418-*  
529 *1419* and *atu1420*), in agreement with its oligomeric state. Similarly, the structure of *Cupriavidus*  
530 *necator* CbnR transcriptional regulator (a tetramer composed of dimer of dimer) from LysR family (PDBs  
531 1IXC and 1IZL (45)) is compatible with an interaction with two DNA binding sites on a bended DNA  
532 fragment, where the authors suggested that the quaternary structure of the CbnR tetramer should be  
533 changed to relax the bent DNA that binds to the CbnR tetramer (45). In contrast to the quaternary  
534 organization of Lac repressor (a tetramer comprising a pair of dimers loosely associated with each other)  
535 which suggests that the structural change of each dimer seems to be able to occur independently,

536 conformational changes of one subunit of Atu1419 and CbnR can be easily propagated to the other  
537 parts of the tetramer through inter-subunit interactions. Noteworthy, single molecule experiments  
538 revealed that a repressor securing a DNA loop is a stronger transcriptional roadblock for RNA  
539 polymerases than one bound to a single DNA site (49).

540 Finally, we investigated the binding between the tetrameric Atu1419 and the Patu1418-1419 region of  
541 370 bp containing two palindromes (190 bp apart) using negative staining electron microscopy. We  
542 measured the size of the protein (~10nM) and the length of the DNA fragment (~125 nM), which are in  
543 good agreement with the expected values (10 nM and 129 nM, respectively Figure 8). We were able to  
544 observe three categories of binding: a tetramer bound to one DNA fragment, two tetramers bound to  
545 one DNA fragment and a tetramer forming a DNA loop (Figure 8). The loops were measured at ~60-65  
546 nM compatible with the length of 190 bp, which separates two palindromes.

## 547 CONCLUSION

548 Hydroxycinnamic acids are involved in the initiation of the plasmid-encoded pathogenicity program of  
549 *A. fabrum* and can be degraded through the expression of the species-specific chromosomal gene  
550 cluster composed of eight genes, which are regulated by two repressors HcaR/Atu1422 and Atu1419.  
551 We have previously shown that HcaR, a dimeric protein from the MarR family, is the transcriptional  
552 repressor of its own transcription, *atu1421* gene and that of the first three genes (*atu1415*, *atu1416* and  
553 *atu1417*) of HCA degradation pathway. Here, we characterized Atu1419 as a transcriptional repressor  
554 of its own repression in addition to two other genes (*atu1418* and *atu1420*). We identified the short  
555 palindromic region composed of 10 base pairs and a degenerated palindrome bound to Atu1419 and  
556 the N5,N10-methylenetetrahydrofolate (MEF) as the effector molecule disrupting Atu1419-DNA  
557 interaction, allowing the expression of the second part of the HCA degradation pathway. Remarkably,  
558 Atu1419 repressor is not regulated by the direct catabolic substrates/intermediates of the pathway. An  
559 unexpected outcome was that Atu1419 is a tetrameric regulator whereas all GntR regulators so far  
560 studied have been shown to be dimeric (20-22). This quaternary structure allows the repressor to bind  
561 two distant DNA sites simultaneously making DNA loop repression (Figure 8) and providing a fine-tune  
562 mechanism in the transcriptional regulation of the appropriate genes at the right time. Our structural  
563 and biophysical study of Atu1419 revealed different structural rearrangements around the fortuitous  
564 citrate bound in the effector binding domain within the tetramer and a double role of the Zn<sup>2+</sup> ion in  
565 protein stability and effector binding. This suggests an induced-allosteric mechanism by MEF, involving  
566 conformational changes “in cascade” which enhance interactions between the DNA binding domain and  
567 the end of the effector binding domain to constrain the flexibility of the HTH motif to prevent it from DNA  
568 binding.

## 569 ACCESSION NUMBERS

570 The atomic coordinates and structure factors have been deposited at the Protein Data bank under PDB  
571 ID 6Z74 and 6ZA0 for Atu1419 in complex with a fortuitous citrate in *P2<sub>1</sub>2<sub>1</sub>2<sub>1</sub>* and *P2<sub>1</sub>2<sub>1</sub>2<sub>2</sub>*, respectively,

572 PDB ID 6ZAB and 6ZA3 for Atu1419 in complex with DNA in *P6<sub>4</sub>22* and *C222<sub>1</sub>*, respectively and PDB  
573 ID 6ZA7 for apo Atu1419.

#### 574 **SUPPLEMENTARY DATA**

575 Supplementary Data are available at NAR online: Supplementary Figures S1 to S9 and Tables S1 to  
576 S3.

#### 577 **ACKNOWLEDGEMENT**

578 We acknowledge SOLEIL for provision of synchrotron radiation facilities (proposals ID 20130869,  
579 20140774, 20150780 and 20170872) in using Proxima beamlines. We are grateful to Nadine Assrir  
580 (ICSN, Gif sur Yvette) and Pascal Retailleau (ICSN, Gif sur Yvette) for access to the CD equipment and  
581 help in data processing. We are grateful to Christophe Velours for performing SEC-MALS experiment  
582 on the Protein-protein interactions platform. We thank the Cell and Tissue Imaging (PICT IBiSA), Institut  
583 Curie, member of the French National Research Infrastructure France-BioImaging (ANR10-INBS-04).  
584 We thank Andrew Saurin for a critical reading of the manuscript.

#### 585 **FUNDING**

586 AV, SM, TM, LV, CL was supported by CNRS (Mission pour l'interdisciplinarité, Agromics 2014-2016).  
587 This work was submitted to fulfill the requirements for a doctorate of biology at ED341-E2M2 from  
588 Université de Lyon, granted from the French Ministère de l'Education Nationale, de l'Enseignement  
589 Supérieur et de la Recherche (T.M). This work has benefited from the I2BC crystallization and Protein-  
590 protein interactions platforms supported by FRISBI ANR-10-INSB-05-01.

591

#### 592 **CONFLICT OF INTEREST**

593 The authors declare that they have no competing interests.

594

595

596 **FIGURES LEGENDS**

597 **Figure 1. (A)** Ferulic acid degradation pathway: a coenzyme A is added to ferulic acid by Atu1416, a  
598 feruloyl-CoA synthase. Feruloyl-CoA is then converted by Atu1417, an enoyl-CoA hydratase, into 4-  
599 hydroxy-3-methoxyphenyl- $\beta$ -hydroxypropionyl (HMPHP)-CoA, which is in turn transformed into vanillic  
600 acid by Atu1415, a phenylhydroxypropionyl-CoA dehydrogenase, and then Atu1421, a 4-hydroxy-3-  
601 methoxyphenyl- $\beta$ -ketopropionyl-CoA (HMPKP)-CoA  $\beta$ -keto-thiolase. The O-demethylase Atu1420  
602 degrades vanillic acid into protocatechuic acid using tetrahydrofolate (H4F) as a cofactor and produces  
603 N5-methyl-tetrahydrofolate (MH4F). Protocatechuic acid enters the cycle of Krebs. Atu1418 enzyme  
604 was proposed to be involved in the recycling of H4F from transformation of MH4F into MEF, a compound  
605 that can be enzymatically or spontaneously converted to H4F (18,50). Dashed arrows indicated putative  
606 reactions based on sequence similarities and references (4,18,44,50). **(B)** Organization of the SpG8-  
607 1b region for which genes expression is regulated by the two transcriptional factors HcaR and Atu1419  
608 (their genes are framed in red). Promoters are shown with small arrows in black for HcaR dependent-  
609 transcription and in blue for putative Atu1419 dependent-transcription indicating the direction of gene  
610 transcription.

611 **Figure 2.** Atu1419 regulation mechanism. **(A)** Gel shift analysis of 30 nM of each promoter region  
612 *Patu1416-1417*, *Patu1418-1419*, *Patu1420*, *PhcaR (atu1422)* incubated without and with 250 nM  
613 tetrameric Atu1419 (ratio protein:DNA of 8.3). *PvirB* was used as a promoter region control. **(B)** In silico  
614 analysis of the *atu1418-1419* and *atu1420* promoter regions performed with the BPROM program (31):  
615 -10 and -35 boxes are underlined, and the palindromic sequences are shown in red. The transcription  
616 initiation sites are shown with an arrow and the translation start sites are indicated in bold. Palindromic  
617 regions are separated by 190 bp in *atu1418-1419* region. **(C)** Gel mobility shift assay analysis of 30 nM  
618 of three parts of the promoter region of *atu1418-1419* containing each one palindrome (P1 or P2) or  
619 none (P3) incubated without and with 250 nM tetrameric Atu1419 (ratio protein:DNA of 8.3).

620 **Figure 3. (A)** Wire representation of Atu1419 tetramer in complex with a fortuitous citrate molecule and  
621 a co-purified Zn<sup>2+</sup> ion, shown as sticks and ball, respectively, bound to the effector binding domain in  
622 the structure at 2 Å resolution (molecule A is in cyan whereas molecules B/C/D in gray). **(B)** Left: ribbon  
623 representation of dimer AB within the tetramer in **A**. The secondary structural elements are indicated in  
624 subunit A and the orange elements form the dimeric interface. The linker joining the N-terminal DNA  
625 binding domain and the C-terminal effector binding domain is shown in black. Right: ribbon  
626 representation of dimer AD within the tetramer in **A**. The secondary structural elements are indicated in  
627 subunit A and the orange elements form the other dimeric interface **(C)** Superposition of the subunits A  
628 in cyan and B in gray of the tetramer in **A** (the subunits B, C, D adopt the same fold). The red parts  
629 indicate major conformational changes between both subunits. A close-up view of the citrate and ion  
630 binding sites in the effector/metal binding domain shown in blue and orange for subunits A and B,  
631 respectively. **(D)** Interactions between the bound citrate in orientation A and in blue/Zn<sup>2+</sup> (blue ball) and  
632 subunit A in cyan. Hydrogen bonds are shown as dashed lines in black (distance below 3.2 Å) and  
633 metal contacts are shown as dashed lines in red. Residues involved in the interactions are labeled and

634 shown as sticks. Citrate is shown in its Fo-Fc omit map contoured at  $4\sigma$  in subunit A. (E) Interactions  
635 between the bound citrate in orientation B and in orange/ $Zn^{2+}$  (orange ball) and subunit B in gray.  
636 Hydrogen bonds are shown as dashed lines in black (distance below 3.2 Å) and metal contacts are  
637 shown as dashed lines in red. Residues involved in the interactions are labeled and shown as sticks.  
638 Citrate is shown in its Fo-Fc omit map contoured at  $4\sigma$  in subunit A.

639 **Figure 4.** Cartoon representation of the tetrameric Atu1419-DNA complex (A) in the  $P6_422$  structure  
640 with the monomer of the asymmetric unit shown in purple. (B) in the  $P2_12_12_1$  structure with the dimer of  
641 the asymmetric unit shown in magenta. (C) Superposition of the DNA binding domains of the dimers  
642 AB of the  $P6_422$  structure in purple and gray for subunits A and B, respectively and of the  $P2_12_12_1$   
643 structure in magenta. The palindromic 10-mer DNA is in green and orange in the  $P6_422$  and  $P2_12_12_1$   
644 structures, respectively. (D) View of the DNA binding domain of the dimer AB of the  $P6_422$  structure in  
645 purple and gray for subunits A and B, respectively bound to the palindromic 10-mer DNA shown in  
646 green. The secondary elements are indicated in subunit A. Arg45 in helix  $\alpha 3$  is the key residue, which  
647 interacts with the essential guanine base at position 3. This residue is shown as sticks. (E) View showing  
648 a close-up of the Atu1419-DNA interface within a monomer and schematic diagram of Atu1419-DNA  
649 contacts. Nucleotide bases that interact with Atu1419 are shown in green. (F) Gel mobility shift assay  
650 analysis of *Patu1420* incubated without and with Atu1419, and with Atu1419 and 100  $\mu M$  citrate (ratio  
651 tetrameric protein:DNA of 8.3). (G) Gel mobility shift assay analysis of *Patu1420s* containing a unique  
652 palindrome or *Patu1420s* AT, in which the palindrome was mutated with the recognized guanine at  
653 position 3 replaced by an adenine and its cytosine partner replaced by a thymine, incubated without  
654 and with Atu1419 (ratio tetrameric protein:DNA of 4.6).

655 **Figure 5.** (A) Cartoon representation of the C-terminal domain except for helix  $\alpha 5$  shown in ribbon of  
656 Atu1419 with a co-purified  $Zn^{2+}$  ion and a close-up view of the  $Zn^{2+}$  binding site. The four amino acid  
657 residues bound to the metal ion (orange ball) are shown as sticks. (B) Superposition of dimers AB of  
658 apo Atu1419 (in orange) and Atu1419-DNA complex (in purple and gray). The DNA is in green. (C)  
659 Close-up view showing the superposition of their DNA binding domains colored as in B with a view at  
660  $90^\circ$ .

661 **Figure 6.** (A) (B) (C) *Patu1418*, *Patu1419* or *Patu1420* expression in *A. fabrum* C58 wild-type strain  
662 compared with that in  $C58\Delta atu1420$  and  $C58\Delta atu1418$  mutants in the presence of ferulic acid. Values  
663 correspond to normalized fluorescence intensity in the presence of ferulic acid corrected by subtracting  
664 values without ferulic acid. Different letters indicate statistical differences between conditions (one-way  
665 ANOVA and Tukey test; P-value=0.05). (D) Gel mobility shift assay analysis of *Patu1420* DNA region  
666 incubated without and with Atu1419 (ratio tetrameric protein:DNA of 17) and N5,N10-  
667 methylenetetrahydrofolate at different concentrations (0 to 300  $\mu M$ ). (E) Gel mobility shift assay analysis  
668 of *Patu1420* DNA region incubated without and with Atu1419, and with Atu1419 and H4F, MH4F or  
669 MEF at 100  $\mu M$ . (F) Differential scanning calorimetry thermograms of apo Atu1419 (black) and Atu1419  
670 in the presence of MEF (magenta). The table below indicates the  $T_m$ . DSC experiments were performed

671 twice. (G) Isothermal titration microcalorimetry (ITC) experiments of Atu1419 towards MEF. The top  
672 panel shows heat differences upon injection of MEF and low panel shows integrated heats of injection  
673 with the best fit (solid line) to a single binding model using Microcal ORIGIN. (H) Control of MEF injection  
674 in the buffer solution by ITC.

675 **Figure 7.** (A) *atu1420* promoter region: -10 and -35 boxes are underlined, the palindromic sequence  
676 and the degenerated palindromic sequence (109 bp apart) are in red. The transcription initiation site is  
677 shown with an arrow and the translation start site is indicated in bold. (B) Gel mobility shift assay  
678 analysis of four parts of the promoter region of *atu1420* containing each one palindrome or one  
679 degenerated palindrome (P1 or P2), or both (P1+P2) or none (P3) incubated without and with 250 nM  
680 or 500 nM tetrameric Atu1419 (ratio protein:DNA of 8.3 or 16.6).

681 **Figure 8.** Interactions between the tetrameric Atu1419 repressor and *Patu1418-1419* region of 370 bp  
682 containing two palindromes separated by 190 bp visualized by electron microscopy and corresponding  
683 model. (A) Image of Atu1419 tetramer as a control, (B) Image of *Patu1418-1419* region as a control,  
684 (C) Image of one tetramer bound to one palindrome only, (D) Image of two tetramers bound each to  
685 one palindrome, (E) Image of one tetramer and a DNA loop.

686

## 687 REFERENCES

- 688 1. Nester, E.W. (2014) Agrobacterium: nature's genetic engineer. *Front Plant Sci*, **5**, 730.  
689 2. Dessaux, Y. and Faure, D. (2018) Niche Construction and Exploitation by Agrobacterium: How  
690 to Survive and Face Competition in Soil and Plant Habitats. *Curr Top Microbiol Immunol*, **418**,  
691 55-86.  
692 3. Meyer, T., Thiour-Mauprivez, C., Wisniewski-Dye, F., Kerzaon, I., Comte, G., Vial, L. and Lavire,  
693 C. (2019) Ecological Conditions and Molecular Determinants Involved in Agrobacterium  
694 Lifestyle in Tumors. *Front Plant Sci*, **10**, 978.  
695 4. Lassalle, F., Campillo, T., Vial, L., Baude, J., Costechareyre, D., Chapulliot, D., Shams, M.,  
696 Abrouk, D., Lavire, C., Oger-Desfeux, C. *et al.* (2011) Genomic species are ecological species  
697 as revealed by comparative genomics in Agrobacterium tumefaciens. *Genome Biol Evol*, **3**,  
698 762-781.  
699 5. Campillo, T., Renoud, S., Kerzaon, I., Vial, L., Baude, J., Gaillard, V., Bellvert, F., Chamignon,  
700 C., Comte, G., Nesme, X. *et al.* (2014) Analysis of hydroxycinnamic acid degradation in  
701 Agrobacterium fabrum reveals a coenzyme A-dependent, beta-oxidative deacetylation pathway.  
702 *Appl Environ Microbiol*, **80**, 3341-3349.  
703 6. Bhattacharya, A., Sood, P. and Citovsky, V. (2010) The roles of plant phenolics in defence and  
704 communication during Agrobacterium and Rhizobium infection. *Mol Plant Pathol*, **11**, 705-719.  
705 7. Guo, M., Huang, Z. and Yang, J. (2017) Is there any crosstalk between the chemotaxis and  
706 virulence induction signaling in Agrobacterium tumefaciens? *Biotechnol Adv*, **35**, 505-511.  
707 8. Parke, D., Ornston, L.N. and Nester, E.W. (1987) Chemotaxis to plant phenolic inducers of  
708 virulence genes is constitutively expressed in the absence of the Ti plasmid in Agrobacterium  
709 tumefaciens. *J Bacteriol*, **169**, 5336-5338.  
710 9. Kape, R., Parniske, M. and Werner, D. (1991) Chemotaxis and nod Gene Activity of  
711 Bradyrhizobium japonicum in Response to Hydroxycinnamic Acids and Isoflavonoids. *Appl*  
712 *Environ Microbiol*, **57**, 316-319.  
713 10. Kalogeraki, V.S., Zhu, J., Eberhard, A., Madsen, E.L. and Winans, S.C. (1999) The phenolic vir  
714 gene inducer ferulic acid is O-demethylated by the VirH2 protein of an Agrobacterium  
715 tumefaciens Ti plasmid. *Mol Microbiol*, **34**, 512-522.

- 716 11. Meyer, T., Renoud, S., Vigouroux, A., Miomandre, A., Gaillard, V., Kerzaon, I., Prigent-  
717 Combaret, C., Comte, G., Morera, S., Vial, L. *et al.* (2018) Regulation of hydroxycinnamic acid  
718 degradation drives *Agrobacterium fabrum* lifestyles. *Mol Plant Microbe Interact.*
- 719 12. Duprey, A., Reverchon, S. and Nasser, W. (2014) Bacterial virulence and Fis: adapting  
720 regulatory networks to the host environment. *Trends Microbiol*, **22**, 92-99.
- 721 13. Valentini, M., Gonzalez, D., Mavridou, D.A. and Filloux, A. (2018) Lifestyle transitions and  
722 adaptive pathogenesis of *Pseudomonas aeruginosa*. *Curr Opin Microbiol*, **41**, 15-20.
- 723 14. Barton, I.S., Fuqua, C. and Platt, T.G. (2018) Ecological and evolutionary dynamics of a model  
724 facultative pathogen: *Agrobacterium* and crown gall disease of plants. *Environ Microbiol*, **20**,  
725 16-29.
- 726 15. Kohler, A.C., Mills, M.J.L., Adams, P.D., Simmons, B.A. and Sale, K.L. (2017) Structure of aryl  
727 O-demethylase offers molecular insight into a catalytic tyrosine-dependent mechanism. *Proc*  
728 *Natl Acad Sci U S A*, **114**, E3205-E3214.
- 729 16. Harada, A., Kamimura, N., Takeuchi, K., Yu, H.Y., Masai, E. and Senda, T. (2017) The crystal  
730 structure of a new O-demethylase from *Sphingobium* sp. strain SYK-6. *FEBS J*, **284**, 1855-  
731 1867.
- 732 17. Parke, D. (1995) Supraoperonic clustering of *pca* genes for catabolism of the phenolic  
733 compound protocatechuate in *Agrobacterium tumefaciens*. *J Bacteriol*, **177**, 3808-3817.
- 734 18. Abe, T., Masai, E., Miyauchi, K., Katayama, Y. and Fukuda, M. (2005) A tetrahydrofolate-  
735 dependent O-demethylase, LigM, is crucial for catabolism of vanillate and syringate in  
736 *Sphingomonas paucimobilis* SYK-6. *J Bacteriol*, **187**, 2030-2037.
- 737 19. Hoskisson, P.A. and Rigali, S. (2009) Chapter 1: Variation in form and function the helix-turn-  
738 helix regulators of the GntR superfamily. *Adv Appl Microbiol*, **69**, 1-22.
- 739 20. Rigali, S., Derouaux, A., Giannotta, F. and Dusart, J. (2002) Subdivision of the helix-turn-helix  
740 GntR family of bacterial regulators in the FadR, HutC, MocR, and YtrA subfamilies. *J Biol Chem*,  
741 **277**, 12507-12515.
- 742 21. Suvorova, I.A., Korostelev, Y.D. and Gelfand, M.S. (2015) GntR Family of Bacterial  
743 Transcription Factors and Their DNA Binding Motifs: Structure, Positioning and Co-Evolution.  
744 *PLoS One*, **10**, e0132618.
- 745 22. Jain, D. (2015) Allosteric control of transcription in GntR family of transcription regulators: A  
746 structural overview. *IUBMB Life*, **67**, 556-563.
- 747 23. van Aalten, D.M., DiRusso, C.C. and Knudsen, J. (2001) The structural basis of acyl coenzyme  
748 A-dependent regulation of the transcription factor FadR. *EMBO J*, **20**, 2041-2050.
- 749 24. Allaway, D., Schofield, N.A., Leonard, M.E., Gilardoni, L., Finan, T.M. and Poole, P.S. (2001)  
750 Use of differential fluorescence induction and optical trapping to isolate environmentally  
751 induced genes. *Environ Microbiol*, **3**, 397-406.
- 752 25. Kabsch, W. (2010) Xds. *Acta Crystallogr D Biol Crystallogr*, **66**, 125-132.
- 753 26. McCoy, A.J., Grosse-Kunstleve, R.W., Adams, P.D., Winn, M.D., Storoni, L.C. and Read, R.J.  
754 (2007) Phaser crystallographic software. *J Appl Crystallogr*, **40**, 658-674.
- 755 27. Blanc, E., Roversi, P., Vornrhein, C., Flensburg, C., Lea, S.M. and Bricogne, G. (2004)  
756 Refinement of severely incomplete structures with maximum likelihood in BUSTER-TNT. *Acta*  
757 *Crystallogr D Biol Crystallogr*, **60**, 2210-2221.
- 758 28. Emsley, P. and Cowtan, K. (2004) Coot: model-building tools for molecular graphics. *Acta*  
759 *Crystallogr. D Biol. Crystallogr.*, **60**, 2126-2132.
- 760 29. Sreerama, N. and Woody, R.W. (2000) Estimation of protein secondary structure from circular  
761 dichroism spectra: comparison of CONTIN, SELCON, and CDSSTR methods with an  
762 expanded reference set. *Anal Biochem*, **287**, 252-260.
- 763 30. Whitmore, L. and Wallace, B.A. (2004) DICHROWEB, an online server for protein secondary  
764 structure analyses from circular dichroism spectroscopic data. *Nucleic Acids Res*, **32**, W668-  
765 673.
- 766 31. Solovyev, V. and Salamov, A. (2011) Automatic Annotation of Microbial Genomes and  
767 Metagenomic Sequences. In *Metagenomics and its Applications in Agriculture, Biomedicine*  
768 *and Environmental Studies. (Ed. R. W. Li) Nova Science Publishers*, 17.
- 769 32. Janin, J., Rodier, F., Chakrabarti, P. and Bahadur, R.P. (2007) Macromolecular recognition in  
770 the Protein Data Bank. *Acta Crystallogr D Biol Crystallogr*, **63**, 1-8.
- 771 33. Xu, Y., Heath, R.J., Li, Z., Rock, C.O. and White, S.W. (2001) The FadR.DNA complex.  
772 Transcriptional control of fatty acid metabolism in *Escherichia coli*. *J Biol Chem*, **276**, 17373-  
773 17379.

- 774 34. Shi, W., Kovacicova, G., Lin, W., Taylor, R.K., Skorupski, K. and Kull, F.J. (2015) The 40-  
775 residue insertion in *Vibrio cholerae* FadR facilitates binding of an additional fatty acyl-CoA  
776 ligand. *Nat Commun*, **6**, 6032.
- 777 35. Gao, Y.G., Suzuki, H., Itou, H., Zhou, Y., Tanaka, Y., Wachi, M., Watanabe, N., Tanaka, I. and  
778 Yao, M. (2008) Structural and functional characterization of the LldR from *Corynebacterium*  
779 *glutamicum*: a transcriptional repressor involved in L-lactate and sugar utilization. *Nucleic Acids*  
780 *Res*, **36**, 7110-7123.
- 781 36. van Aalten, D.M., DiRusso, C.C., Knudsen, J. and Wierenga, R.K. (2000) Crystal structure of  
782 FadR, a fatty acid-responsive transcription factor with a novel acyl coenzyme A-binding fold.  
783 *EMBO J*, **19**, 5167-5177.
- 784 37. Lord, D.M., Uzgoren Baran, A., Soo, V.W., Wood, T.K., Peti, W. and Page, R. (2014)  
785 McbR/YncC: implications for the mechanism of ligand and DNA binding by a bacterial GntR  
786 transcriptional regulator involved in biofilm formation. *Biochemistry*, **53**, 7223-7231.
- 787 38. Zheng, M., Cooper, D.R., Grosseohme, N.E., Yu, M., Hung, L.W., Cieslik, M., Derewenda, U.,  
788 Lesley, S.A., Wilson, I.A., Giedroc, D.P. *et al.* (2009) Structure of *Thermotoga maritima* TM0439:  
789 implications for the mechanism of bacterial GntR transcription regulators with Zn<sup>2+</sup>-binding  
790 FCD domains. *Acta Crystallogr D Biol Crystallogr*, **65**, 356-365.
- 791 39. Pinheiro, J., Lisboa, J., Pombinho, R., Carvalho, F., Carreaux, A., Brito, C., Pontinen, A.,  
792 Korkeala, H., Dos Santos, N.M.S., Morais-Cabral, J.H. *et al.* (2018) MouR controls the  
793 expression of the *Listeria monocytogenes* Agr system and mediates virulence. *Nucleic Acids*  
794 *Res*, **46**, 9338-9352.
- 795 40. Otani, H., Stogios, P.J., Xu, X., Nocek, B., Li, S.N., Savchenko, A. and Eltis, L.D. (2016) The  
796 activity of CouR, a MarR family transcriptional regulator, is modulated through a novel  
797 molecular mechanism. *Nucleic Acids Res*, **44**, 595-607.
- 798 41. Cogan, D.P., Baraquet, C., Harwood, C.S. and Nair, S.K. (2018) Structural basis of  
799 transcriptional regulation by CouR, a repressor of coumarate catabolism, in  
800 *Rhodospseudomonas palustris*. *J Biol Chem*, **293**, 11727-11735.
- 801 42. Danenberg, P.V., Gustavsson, B., Johnston, P., Lindberg, P., Moser, R., Odin, E., Peters, G.J.  
802 and Petrelli, N. (2016) Folates as adjuvants to anticancer agents: Chemical rationale and  
803 mechanism of action. *Crit Rev Oncol Hematol*, **106**, 118-131.
- 804 43. Jagerstad, M. and Jastrebova, J. (2014) 5,10-Methylene-tetrahydrofolate dissociates into  
805 tetrahydrofolate and formaldehyde at physiological pH and acidic pH, typical conditions used  
806 during sample extraction and LC-MS/MS analysis of biological samples. *Biomed Chromatogr*,  
807 **28**, 1041-1042.
- 808 44. Feirer, N., Xu, J., Allen, K.D., Koestler, B.J., Bruger, E.L., Waters, C.M., White, R.H. and Fuqua,  
809 C. (2015) A Pterin-Dependent Signaling Pathway Regulates a Dual-Function Diguanylate  
810 Cyclase-Phosphodiesterase Controlling Surface Attachment in *Agrobacterium tumefaciens*.  
811 *mBio*, **6**, e00156.
- 812 45. Muraoka, S., Okumura, R., Ogawa, N., Nonaka, T., Miyashita, K. and Senda, T. (2003) Crystal  
813 structure of a full-length LysR-type transcriptional regulator, CbnR: unusual combination of two  
814 subunit forms and molecular bases for causing and changing DNA bend. *J Mol Biol*, **328**, 555-  
815 566.
- 816 46. Amouyal, M., Mortensen, L., Buc, H. and Hammer, K. (1989) Single and double loop formation  
817 when deoR repressor binds to its natural operator sites. *Cell*, **58**, 545-551.
- 818 47. Bylino, O.V., Ibragimov, A.N. and Shidlovskii, Y.V. (2020) Evolution of Regulated Transcription.  
819 *Cells*, **9**.
- 820 48. Lewis, M., Chang, G., Horton, N.C., Kercher, M.A., Pace, H.C., Schumacher, M.A., Brennan,  
821 R.G. and Lu, P. (1996) Crystal structure of the lactose operon repressor and its complexes with  
822 DNA and inducer. *Science*, **271**, 1247-1254.
- 823 49. Voros, Z., Yan, Y., Kovari, D.T., Finzi, L. and Dunlap, D. (2017) Proteins mediating DNA loops  
824 effectively block transcription. *Protein Sci*, **26**, 1427-1438.
- 825 50. De Brouwer, V., Zhang, G.F., Storozhenko, S., Straeten, D.V. and Lambert, W.E. (2007) pH  
826 stability of individual folates during critical sample preparation steps in prevision of the analysis  
827 of plant folates. *Phytochem Anal*, **18**, 496-508.

828

**Table 1.** Crystallographic data and refinement parameters

	Zn <sup>2+</sup> SAD	Atu1419 Citrate	Atu1419 Citrate	Atu1419-DNA#	Atu1419-DNA§	Apo Atu1419†
PDB code		<b>6Z74</b>	<b>6ZA0</b>	<b>6ZAB</b>	<b>6ZA3</b>	<b>6ZA7</b>
Wavelength (Å)	1.282290	0.97541	0.978570	1	1	0.97934
Crystallization conditions	5% PEG 4K, 0.2 M AS, 0.1 M Na-Citrate pH 5.6	5% PEG 4K, 0.2 M AS, 0.1 M Na-Citrate pH 5.6	5% PEG 4K, 0.2 M AS, 0.1 M Na-Citrate pH 5.6	10% Terbutanol, 0.1 M NaCitrate pH 5.6, 2 mM MgCl <sub>2</sub>	25% PEG 400, 0.1 M MES pH 6.7, 0.2 M Na-Acetate	12% PEG 4K, 0.2 Ammonium Sulfate, 0.1 M Tris/HCl pH 8.5
Za	4	4	2	1	2	4
Space group	<i>P2<sub>1</sub>2<sub>1</sub>2<sub>1</sub></i>	<i>P2<sub>1</sub>2<sub>1</sub>2<sub>1</sub></i>	<i>P2<sub>1</sub>2<sub>1</sub>2</i>	<i>P6<sub>4</sub>22</i>	<i>C222<sub>1</sub></i>	<i>P2<sub>1</sub></i>
Cell parameters (Å, °)	a= 77.4 b= 114.1 c= 130.5	a= 77.2 b= 113.7 c= 130.5	a= 72.2 b= 145.6 c= 41.2	a= 179.5 b= 179.2 c= 96.8	a= 62.4 b= 112.4 c= 179.6	a= 52.1 b= 79.0 c= 140.6 β= 95.1
Resolution (Å)	49.8-2.35 (2.42-2.35)	45.6-2 (2.12-2)	24.0-1.65 (1.69-1.65)	45.61-2.8 (2.87-2.8)	47.64-2.0 (2.05-2.0)	43.38-2.34 (2.41-2.34)
No. of observed reflections	518098 (29677)	467551 (72154)	239555 (17376)	444041 (30119)	376669 (23170)	504810 (31752)
No. of unique reflections	48018 (3262)	78344 (12280)	51917 (3674)	23089 (1642)	43067 (3095)	47943 (3255)
Completeness (%)	99.4 (92.1)	99.6 (98.1)	97.9 (95.8)	99.7 (88.4)	99.9 (99.1)	99.4 (92.3)
Completeness Staraniso (%)				68.7 (11.9)	97.7 (79.3)	71.5 (30.6)
<i>R</i> <sub>sym</sub> (%)	8.8 (78.6)	12 (155.5)	8.1 (127.3)	11.6 (236.4)	8.6 (190.3)	10.9 (128.8)
<i>R</i> <sub>pim</sub> (%)	2.8 (26.6)	5.4 (78.1)	4.2 (64.4)	2.7 (57.7)	3.1 (79.3)	3.5 (41.5)
<i>I</i> / <i>σ</i> ( <i>I</i> )	18 (2.3)	10 (1.12)	10.7 (1.1)	18.8 (1.1)	13.7 (0.9)	13.0 (1.4)
CC <sub>1/2</sub>	0.999 (0.809)	0.998 (0.582)	0.999 (0.461)	0.999 (0.469)	0.999 (0.421)	0.999 (0.696)
<i>R</i> <sub>cryst</sub> (%)		19.1	16.9	18.8	19.2	19.4
<i>R</i> <sub>free</sub> (%)		21.4	18.9	19.9	22.8	22.2
rms bond deviation (Å)		0.01	0.001	0.009	0.01	0.009
rms angle deviation (°)		0.99	0.95	1	1	1.02
Average B (Å <sup>2</sup> )						
Protein A/B/C/D		42/53.1/60/57.5	27.9/29.2	86.4	50.7/50.1	66.2/74.3/73.2/80.8
Zn <sup>2+</sup>		35/41.4/39.7/45.2	18.3/18.6	106.9	43.3/46.2	46.2/63.2/69.3/66.6
citrate		44.4/45.2/44.5/45.7	23.1/22	127.9		
DNA				65.3	60.2	
solvent		50.5	36.7	56.3	48.	50
<sup>a</sup> Clashscore		4.56	1.6	3.2	2.11	2.88
MolProbity score		1.51	0.93	2.07	1.24	1.38
<sup>a</sup> Ramachandran plot (%)						
Favoured		99.36	98.73	94.94	98.73	98.2
Outliers		0	0	0	0	0.21

Values for the highest resolution shell are in parentheses. CC<sub>1/2</sub> = percentage of correlation between intensities from random half-dataset

<sup>a</sup>Calculated with MolProbity

Numbers in italic account for statistical values after ellipsoidal mask application by Staraniso.

# A dataset collected from a crystal, which diffracted anisotropically to 3.4 Å along *b*\* and 0.894*a*\* - 0.447*b*\* and 2.7 Å along *c*\*

† Two datasets collected from a crystal, which diffracted anisotropically to 3.2 Å along 0.81*a*\* - 0.58*c*\*, 2.3 Å along *b*\* and 2.2 Å along *c*\*

§ One dataset collected from a crystal, which diffracted anisotropically to 2.02 Å along *a*\*, 1.99 Å along *b*\* and 1.95 Å along *c*\*

**Table 2.** SpG8 1-b genes expression in the wild-type (WT) and C58 $\Delta$ *atu1419* strains. Values refer to fold change at 24 hours obtained by comparison of genes expression in the WT C58 strain with and without 750  $\mu$ M of ferulic acid and correspond to the mean of three biological replicates with at least six technical replicates. Fold change at 24 hours without ferulic acid was obtained by comparison of genes expression in the C58 $\Delta$ *atu1419* and the WT strains and corresponds to the mean of at least two biological replicates and six technical replicates. Empty pOT1e corresponds to plasmid without any promoting region before the *egfp* gene in order to measure basal expression of the system.

<b>Genes</b>	<b>Fold change C58 WT in the presence/in the absence of ferulic acid</b>	<b>Fold change C58<math>\Delta</math><i>atu1419</i>/WT in the absence of ferulic acid</b>
<i>Patu1416</i>	2.53	0.63
<i>Patu1418</i>	1.44	3.67
<i>Patu1419</i>	1.81	3.92
<i>Patu1420</i>	3.31	1.58
Empty pOT1e	1.12	0.97

Figure 1.

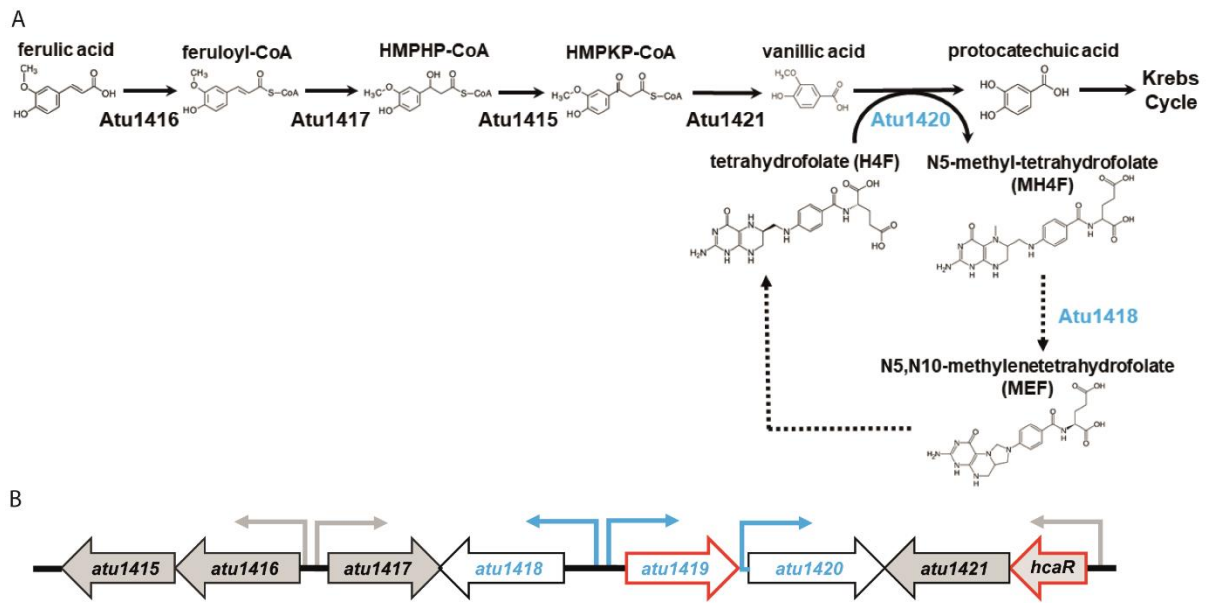


**Figure 2.**

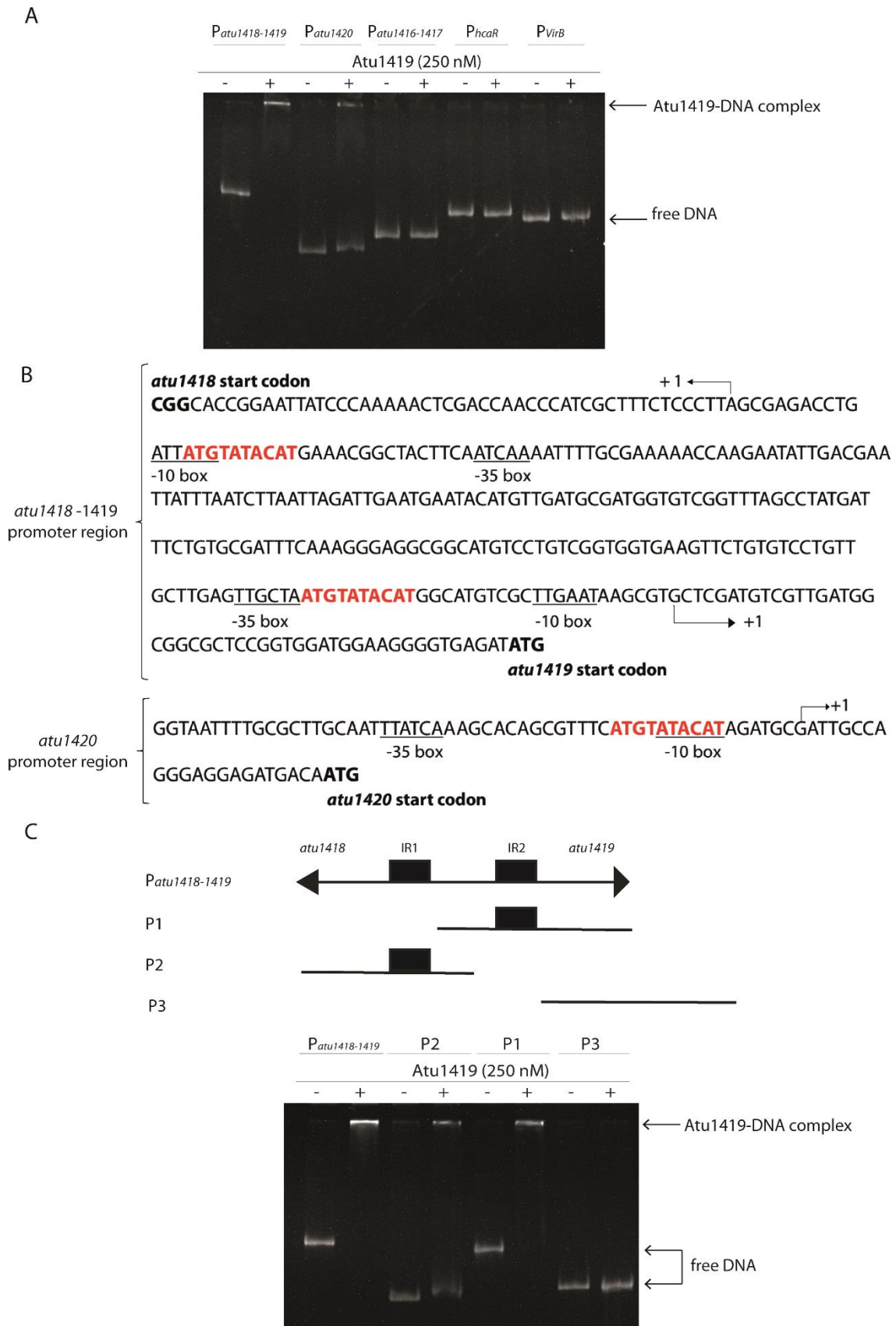


**Figure 3.**

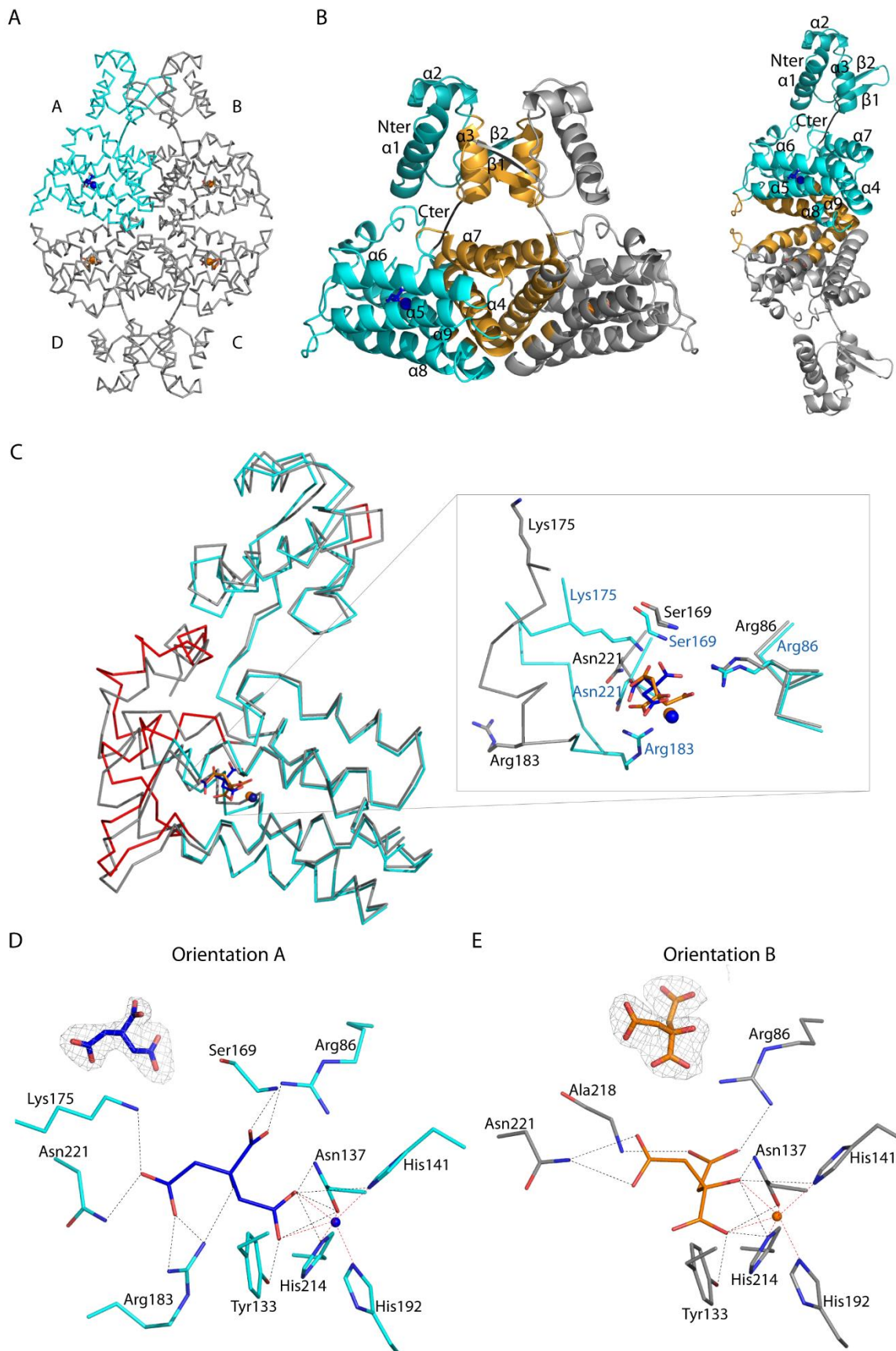


**Figure 4.**

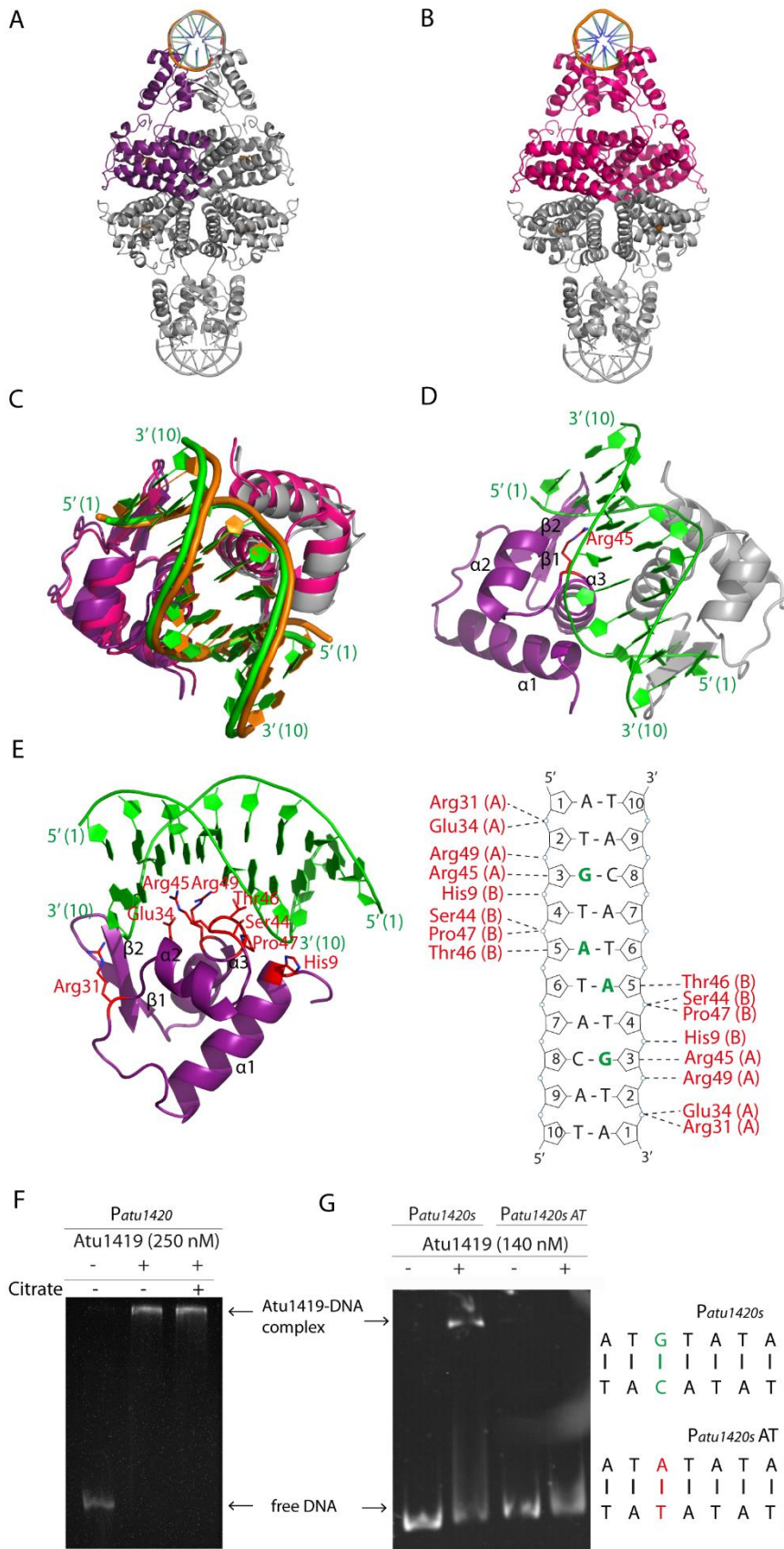
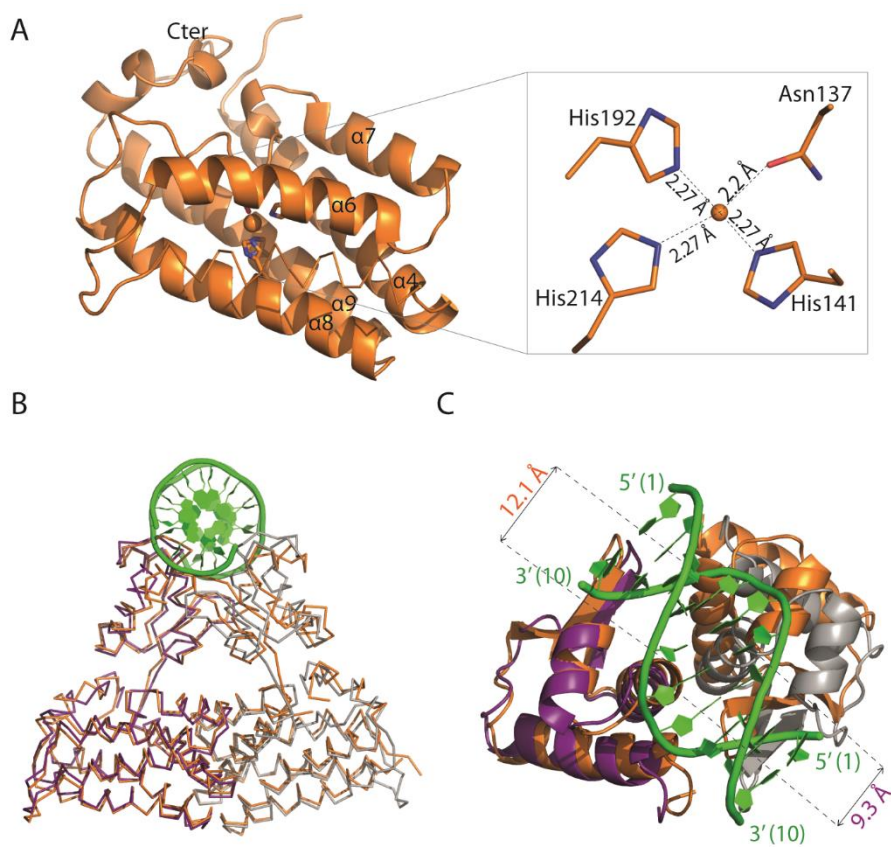
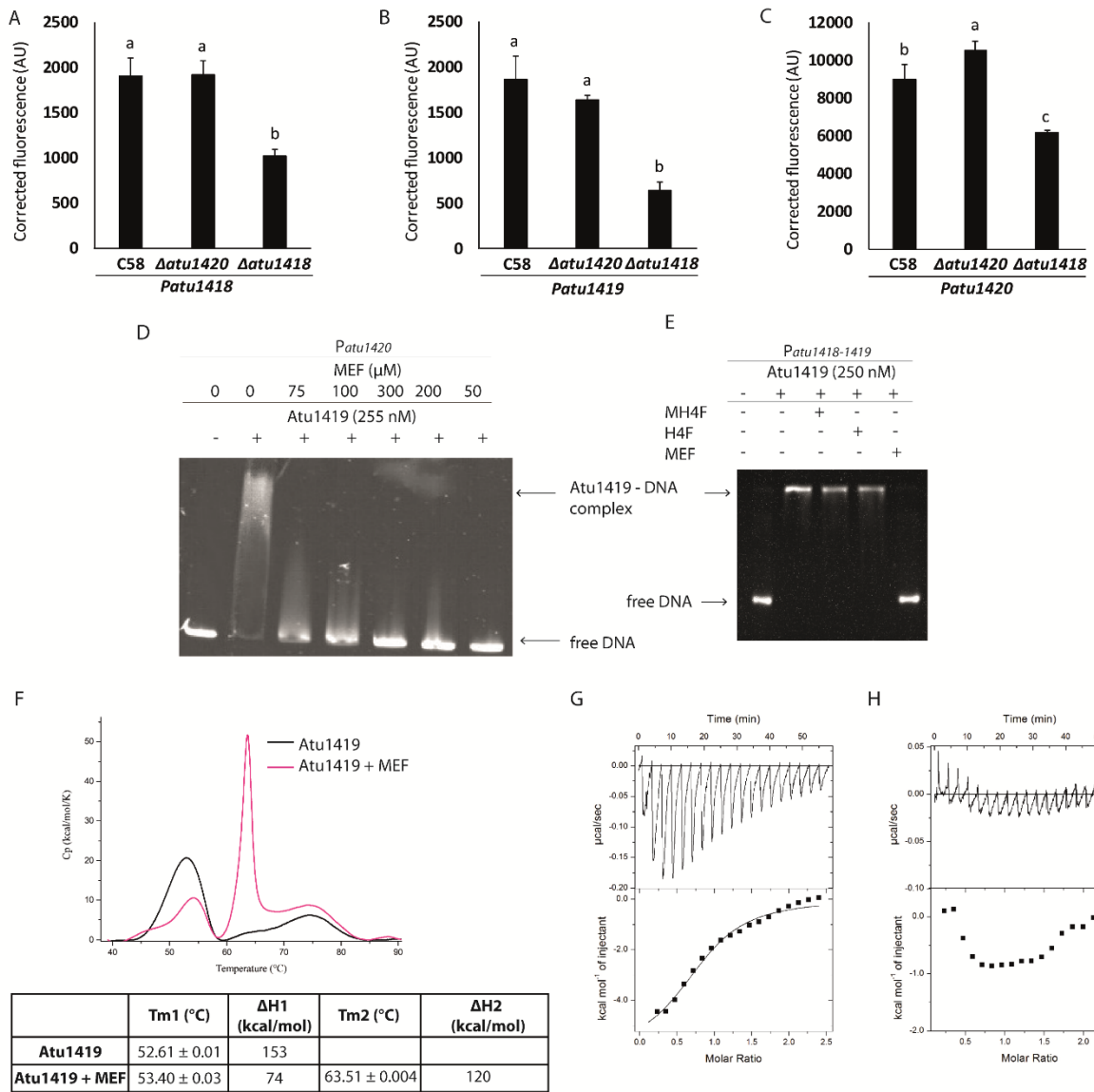


Figure 5.



829

830 **Figure 6.**



831

832

833

834 **Figure 7**

